University of Southern Denmark

Ph. D. Thesis

Manipulation of the Light-Emission of Organic Nanofibers by Structure Formation

Author:
Ralf Frese

Supervisor:
Prof. Dr. H.-G. Rubahn

June 2, 2008

Mads Clausen Institute / NanoSYD
Alsion 2
6400 Sønderborg

Denmark

Syddansk Universitet

NanoSYD

Contents

Chapter 1

Introduction

1.1 Motivation

In the last decades advanced material processing made it able to produce a series of new materials with novel properties. On the one hand the control of growth and fabrication processes provided the possibility to produce structures in the regime of nanometers. On the other hand organic chemistry is able to produce novel materials from designed molecules.

Oligomeres from para-phenylenes are a series of novel materials whith promising properties. The molecules itself are rod-like shaped with a delocalized Π-electron system. Their blue fluorescence make them promissing candidates for optical devices like active layers in organic light emitting diodes or lasers [36].

It has been shown, that under certain conditions, para-hexa-phenylene molecules (p6P) form aggregates with dimensions of a few tens nanometers in height, a few hundreds nanometers in width and up to several hundret micrometers in length. These nanofibers offer access to the sub-micron regime due to their cross-section, as well as the macroscopic world due to their length.

It has been shown in recent experiments,, that these fiber act as optical waveguides[6] and show random lasings[2]. This enables them to act as an interesting model system for sub-wavelength optics, and as an element, which can localy deliver light for nano-optic applications[4].

In this thesis it is investigated how to utilize these structures for future application. In the first part, a mathematical model is developed to numerically calculate the optical fields in these structures. The model is based on the Helmholz equation in dielectric materials and solved by a finite element approach. The second part demonstrates how to change properties of organic nanofibers by influencing the growth. In the last part of this thesis,

the set-up of an excimer laser material treatment station is described. By utilizing a deep-UV high-power laser, it is possible to structure materials in the sub-micron regime.

1.2 Organic Nanofibers

Organic nanofibers are a class of new material, that offer a cross-section in the sub-micrometer regime and an elongation of macroscopic sizes. The nanofibers are produced in a bottom-up process, by self-assembly. Classical methods of micro-structuring utilize top-down methods like photolithography. In contrast, the principle behind this structure formation is based on an interaction on a molecular level, resulting in parallel production of millions of fibers in a single process step.

The growth of organic nanofibers is done on muscovite mica, which is a silicate mineral with a highly perfect basal cleavage. In the cleavage process, potassium ions are removed from the cleavage plane, resulting in strong surface-dipole moments. Freshly cleaved mica sheets are transferred in high vacuum chambers, where they are attached to heating elements.

Inside the vacuum chambers organic material is evaporated from a Knudsen cell at low evaporation rates. The molecules forming organic nanofibers have a delocalized Π-electron system allowing them to align themself along the surface dipole moments by a dipole induced-dipole interaction.

Due to the heating, the molecules have a high mobility on the surface and form clusters. If a critical cluster size is exceeded, the clusters begin assimilating other clusters and start growing in a direction perpendicular to the long fiber axis, maintaining their dimensions in their cross-section and only growing in length. (The exact angle is dependent on the dipole moment of the used molecule and can vary between different materials) [27].

The orientation of the dipole moments is determining the orientation of the organic nanofibers. Depending on the quality of the muscovite mica, the domains in which the dipole moments are pointing in the same direction can reach sizes of the order of cm^2. In the case of para-hexa-phenylene, needle-lengths of the size of the domain can be achieved. The evaporation process results in an array of parallel alligned organic fibers made of single-crystalline organic material.

A direct influence of the crystallinity and the orientation of the molecules is that the fluorescence of the needles is strongly polarized. Due to their alligned electron system, organic nanofibers offer also high electron mobilities [28]. By changing the chemical structure of the molecules, it is possible to design their optical non-linear response and use them as sub-micron frequency doublers [3]

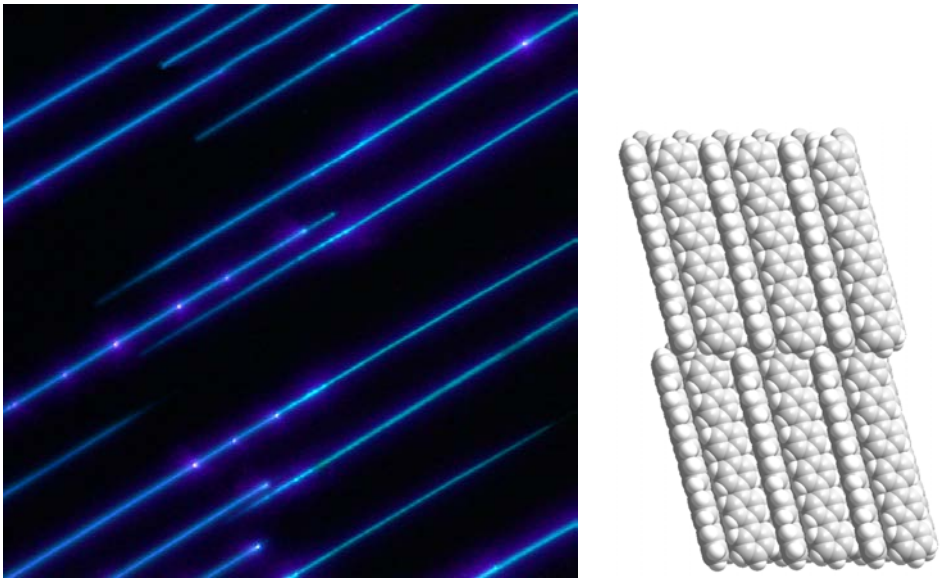

(a) (b)

Figure 1.1: Figure (a) shows a fluorescence microscopy image of a typical p6p sample after growth. Figure (b) is an illustration of the molecular orientation within the crystal structure of a nanofiber.

It has been demonstrated, that p6P-nanofibers act as optical waveguides. This can be observed by locally exciting the fibers with UV-light to fluorescence. After the evaporation process it can happen, that due to thermal stress between the substrate and the nanofiber, a fiber breaks along the fiber axis. These cracks can be used as local probes, scattering the guided light. By observing the attenuation of the guided fluorescence along the fiber axis, it was possible to extract the imaginary part of the dielectric fuction. Francesco Quochi[32] showed, that it is possible to excite the fluorescence by two-photon excitation in a population inverted state. The guided fluorescence was reflected on such thermal breaks and amplified within the fiber axis. It was possible to observe optical gain narrowing of the emitted light of one single fiber[2].

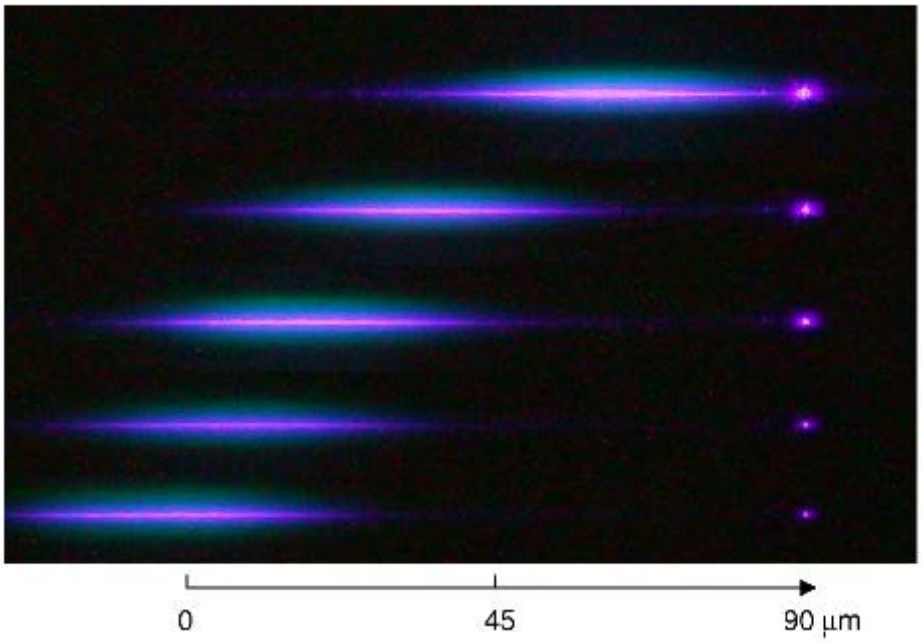

Figure 1.2: Demonstration of the waveguiding properties of organic nanofibers. Nanofibers are locally excited by UV-illumination (left area). The guided light propagates along the needle. A local break in the needle, seen as bright spot on the right, can be used to probe the propagating light[5].

The geometry of the organic nanofibers can be controlled within boundaries, by altering the growth parameters like substrate temperature or evaporation rate[24]. A method of in-situ structuring of the growth process is to localy vary the substrate temperature, for example by laser-heating[11].

A common disadvantage of most self-assembled materials is their permanent attachement to their growth susbtrate. In the case of organic nanofibers, it is possible to transfer the aggregate from the susbtrate to any other surface. This has been demonstrated for the transfer of individual nanofibers in a liquid assisted process [20], or for a bulk transfer by stamping, which is preserving the parallel orientation of the nanofibers[19].

Being able to utilize materials other than muscovite mica, optical investigations can be performed on optical grade substrates like fused silica.

Chapter 2

Simulation of Optical Fields

In the middle of the 19th century James Clerk Maxwell formulated a set of equations, which describe the fundamental theory of electro-magnetics. With help of this theory it is possible to describe electro-magnetic waves covering the range from radio signals through microwaves and optical light to x-ray and gamma radiation.

The Maxwell equations are a set of four partial differential equations (PDEs), which can be analytically solved only for the simplest geometries. Simplifications and approximations have to be applied to calculate common problems, resulting in specialized theories. Paraxial optics and Fraunhofer's or Fresnel's diffraction theory are examples for this. Most theories predict how the optical fields behave far away from objects in the so-called 'far-field'. Close to scattering and refracting objects the electro-magnetic fields behave differently, and show components, that only exist in the near-field[44].

With access to novel techniques and increased computational powers, Maxwell's equation still offer deep insight in the nature of optical phenomena. For example the development of scanning probe microscopy allows one to bring a small optical fiber in the proximity of an object (some nm) and probe the electromagnetic field locally, with a resolution much higher than the diffraction limit.

In this chapter the behavior of structures with lateral dimensions smaller than the wavelength is investigated. As indicated in chapter 1.2, organic nanofibers can be used to investigate near-field optics. Their ability to guide light waves can be applied to future concepts of local light delivery and their optical properties make them promising candidates as active elements in future applications and devices. To get a step closer to implement nanofiber in devices, a theoretical model for electro-magnetic waves in nanofibers is presented and the light-guiding properties are investigated.

2.1 Helmholtz Equation for dielectric Media

The model, which is going to be introduced here, is based on Helmholtz' formulation of the propagation of waves. Since these equations are based on the Maxwell equations it is important to derive the dependencies between Helmholtz and Maxwell equations and discuss if assumptions are fulfilled in both formalisms.

The four Maxwell equations in differential form are:

$$\nabla \cdot \vec{D} = \rho \tag{2.1}$$

$$\nabla \cdot \vec{B} = 0 \tag{2.2}$$

$$\nabla \times \vec{E} = -\frac{\partial}{\partial t}\vec{B} \tag{2.3}$$

$$\nabla \times \vec{H} = \vec{j} + \frac{\partial}{\partial t}\vec{D} \tag{2.4}$$

where $\vec{E}$ is the electrical Field, $\vec{B}$ is the magnetic flux density. The dielectric displacement field $\vec{D}$ and the magnetic field strength $\vec{H}$ are related to the former fields by

$$\vec{D} = \epsilon\vec{E} = \epsilon_0\epsilon_r\vec{E} \tag{2.5}$$

$$\vec{B} = \mu\vec{H} = \mu_0\mu_r\vec{H} \tag{2.6}$$

The dielectric permittivity ϵ and magnetic permeability μ are depending on the environment. These are strongly affected by material, and normally expressed by the macroscopic material constants μ_r and ϵ_r which describe the feedback of atoms and molecules in the field. The dimensions of the structure and fields are in the mesoscopic regime, that means of the size in the order of the wavelength. This regime is dominated by effects of the optical near-field, but it is several orders of magnitude larger before the permittivity and permeability have to be modeled on an atomic level. Nevertheless these values of permittivity and permeability depend on the materials of the modeled system and can take diffrent values in diffrent regions of the geometry.

The materials we want to investigate are insulators and organic substances. Organic materials have a magnetic permeability that does not differ much from the vacuum-permeability. Therefore we set $\mu_r \approx 1$ and simplify:

$$\nabla \times \vec{B} = \mu \left(\nabla \times \vec{H} \right) \tag{2.7}$$

$$\nabla \cdot \vec{B} = \mu \left(\nabla \cdot \vec{H} \right) \tag{2.8}$$

In contrast, the electric permittivity depends on the material and can change rapidly over boundaries between two materials. In other words, the permittivity is depending on the location, and we cannot neglect these changes in the gradient, we have to extract

$$\nabla \vec{D} = (\nabla \epsilon) \cdot \vec{E} + \epsilon \left(\nabla \vec{E} \right) \tag{2.9}$$

$$\nabla \times \vec{D} = (\nabla \epsilon) \times \vec{E} + \epsilon \times \left(\nabla \vec{E} \right) \tag{2.10}$$

Another approximation is based on our interest in the dynamics of the system. Since the equations are linear, we can neglect static currents and charges and super-impose the solution of the static fields later. Also since no conductors are present (μ would significantly differ from the vacuum permeability), we also do not include time varying charges or currents. Therefore a charge and current free system with $\rho = 0$ and $\vec{j} = 0$ is considered.

With these assumptions we can combine the four Maxwell equations 2.1 of first order into a set of two second-order differential equations. The electrical field is described by:

$$\begin{aligned} -\nabla \times \left(\nabla \vec{E} \right) &= \nabla \left(\frac{\partial}{\partial t} \vec{B} \right) \\ \Delta \vec{E} - \nabla \left(\nabla \vec{E} \right) &= \frac{\partial}{\partial t} \left(\nabla \times \mu \vec{H} \right) \\ \Delta \vec{E} + \nabla \left(\frac{1}{\epsilon} \vec{E} \nabla \epsilon \right) &= \mu \frac{\partial^2}{\partial t^2} \vec{D} \\ \Delta \vec{E} + \nabla \left(\frac{1}{\epsilon} \vec{E} \nabla \epsilon \right) &= \mu \epsilon \frac{\partial^2}{\partial t^2} \vec{E} \end{aligned} \tag{2.11}$$

The magnetic fields by:

$$\begin{aligned} -\nabla \times \left(\nabla \times \vec{H} \right) &= -\nabla \left(\frac{\partial}{\partial t} \vec{D} \right) \\ \Delta \vec{H} &= -\frac{\partial}{\partial t} \nabla \epsilon \times \vec{E} + \epsilon \frac{\partial^2}{\partial t^2} \vec{B} \end{aligned} \tag{2.12}$$

Finite Differences Time Domain (FTDT) models utilize this approach. A discretization in space and time would be needed to implement that model, with a requirement of four dimensions. The computational power needed to solve such models is high and can normally only handled by super-computers or computer-clusters. To reduce the computational amount to solve this model, we switch from the time domain to the frequency domain.

By using the ansatz $\tilde{E} = \exp(i\omega t)\vec{E}$ and $\tilde{H} = \exp(i\omega t)\vec{H}$ one can eliminate the dependence in time. Combined with equations 2.11 and 2.12 the Helmholtz equations in dielectric media is derived.

$$\Delta \tilde{E} + \mu\epsilon\omega^2 \tilde{E} = \nabla \left(\frac{1}{\epsilon} \nabla \epsilon \tilde{E} \right) \tag{2.13}$$

$$\Delta \tilde{H} + \mu\epsilon\omega^2 \tilde{H} = i\omega \left(\nabla \epsilon \right) \times \tilde{E} \tag{2.14}$$

This form of the Helmholtz equations differs from the commonly used Helmholtz equation by the right hand side of the equal signs. In the case of dielectric media the two equations are coupled, causing more difficulties in finding a solution[26].

Modeling such a system with FEM methods requires two times as large vectors as for a system with uncoupled equations. The resulting matrices in the simulation scale with four times the number of nodes. In our case, we are interested in structures that form sharp interfaces. The material functions can be assumed to jump in value across an interface. The resulting discontinuity causes the gradient of the permittivity to be undefined.

In limiting approximation, the discontinuity can be expressed by a delta functional. Following this argumentation, it is possible to solve the Helmholtz equations inside one domain and couple them by appropriate boundary conditions to the other domains. Even for simple two dimensional geometries this system cannot be solved analytically and the coupling between the domains has to be extrapolated[42].

Finite Element methods allow to incoperate the coupling between different domains in the solver and find solutions of 2.11. The boundary conditions that couple the fields at an interface are well known. Since we consider only non-conducting dielectric media, we have no surface charges or currents present, and the interface conditions can be formulated as:

$$(\vec{D}_2 - \vec{D}_1) \cdot \vec{n}_{21} = 0 \tag{2.15}$$

$$(\vec{E}_2 - \vec{E}_1) \times \vec{n}_{21} = 0 \tag{2.16}$$

Due to the same permeability, the magnetic fields stay continuous over the boundary.

This equation is the fundamental of the used computational model, that describes the electro-magnetic field of the structures [16].

The following list summarizes the approximations applied to the model:

- charge and current free space
- no influence from atomic sized fluctuations in material constants
- magnetic permeability is equal to that of vacuum
- discrete interfaces

2.1.1 Finite Elements Method

The Helmholtz equation is a partal differential equation of second order. Analytical solutions in closed-form are only known for simple geometries with defined boundary conditions. The set of boundary conditions is an important factor for finding a solution. For example, a rectangular geometry with Dirichlet boundary conditions (metallic, hollow waveguide) can be described analytically. In case of mixed boundary conditions (2-dimensional dielectric slab), an analytical solution cannot be formulated anymore. Analytical approximations may be applied to describe the behavior [15], but to calculate the electrical field distribution ab-initio in such systems, numeric solvers are needed.

One kind of numeric solving algorithms is based on the method of finite elements (FEM). In this method the space is divided into individual elements of finite size. For example, a circle can be approximated by a polygon, where each segment would represent an element. The strategy is to find an simple approximation of the electro-magnetic field in each element that solves the underlying equation in a general form. The discrete elements are afterward stitched together, in a way that their combination represents the approximate solution.

The basic idea of the finite element method is, that a field u in a domain Ω can be represented by an orthonormal base Φ_n in the space of functions L^2.

$$u(x) = \sum_n u_n \Phi(n)(x) \tag{2.17}$$

Each factor u_n can be expressed by the scalar product of the space L^2

$$u_n =< u, \Omega_n >= \int_\Omega \bar{u}(x)\Phi_n(x)\mathrm{d}x \tag{2.18}$$

In the case of a linear subspace $X \subset L^2$ it can be derived from the lemma of Rietz, that the vector u is composed by a sum of a vector $f_{\|} \in X$ in the

subspace and an orthogonal complement $u_\perp \in \bar{X}$, which satisfy.

$$\|u_\perp\| = min \Leftrightarrow f_\parallel = \sum_{\Phi_n \in X} \bar{u}(x)\Phi_n \tag{2.19}$$

In the formalism of function theory, a differential equation is described by an operator in the function space. $L : \Omega \to \Omega$. The Helmholtz and Maxwell equations are linear operators, and the differential equation can be written as:

$$Lu = f \tag{2.20}$$

where u is a solution of this equation. It can be shown, that u is a solution if and only if the following relation is fullfilled for all testfunction v.

$$< Lu, v >=< f, v > : \forall v \in \Omega \tag{2.21}$$

Other pre-requirements influencing the solution of the system are the applied boundary conditions. Two kinds of boundary conditions are considered here:

$$u = g \qquad \text{on } \partial\Omega_D \text{ (Dirichlet boundary conditions)} \tag{2.22}$$

$$\frac{\partial}{\partial n}u - iku = 0 \qquad \text{on } \partial\Omega_S \text{ (Sommerfeld boundary conditions)} \tag{2.23}$$

Galerkin used these correlations and formulated a strategy for finding a solution of a differential equation. The first step in adapting this strategy is to formulate the Helmholtz equation in its weak form. The weak form of a PDE is defined as a bi-linear form in u and the test function v[43]. In the case of the Helmholtz equation the weak form is:

$$-\nabla \cdot \nabla u - k^2 u = f \tag{2.24}$$

$$\int_\Omega -\bar{v}\nabla \cdot \nabla u d\Omega - \int_\Omega k^2 \bar{v} u d\Omega = \int_\Omega \bar{v} f d\Omega \tag{2.25}$$

$$\int_\Omega \nabla u \nabla \bar{v} - k^2 u \bar{v} d\Omega - ik \int_{\partial\Omega_S} u \bar{v} d\Omega = \int_\Omega f \bar{v} d\Omega \tag{2.26}$$

Since we are operating in a linear space, we can express each function as a sum of its orthogonal decomposition as described in equation 2.17. This

form allows us to approximate the solution by the lemma of Rietz 2.19. The only difference between an exact and an approximated solution is, that in the case of the approximation, the testfunctions and solutions are constrained to the subspace.

The different terms in the weak formulation 2.24 are then expressed by:

$$\int_\Omega \nabla u \nabla \bar{v} \ \mathrm{d}\Omega = \int_\Omega \left(\sum_i u_i \nabla \Phi_i \right) \left(\sum_j v_j \nabla \Psi_j \right) \ \mathrm{d}\Omega \tag{2.27}$$

$$\int_\Omega k^2 u \bar{v} \ \mathrm{d}\Omega = \int_\Omega \left(\sum_i u_i \Phi_i \right) \left(\sum_j v_j \Psi_j \right) \ \mathrm{d}\Omega \tag{2.28}$$

$$ik \int_{\partial\Omega_S} u \bar{v} \ \mathrm{d}\Omega = ik \int_{\partial\Omega} \left(\sum_i u_i \Phi_i \right) \left(\sum_j v_j \Psi_j \right) \mathrm{d}\Omega \tag{2.29}$$

$$\int_\Omega f \bar{v} \ \mathrm{d}\Omega = \int_\Omega \left(\sum_i f_i \Phi_i \right) \left(\sum_j v_j \Psi_j \right) \mathrm{d}\Omega \tag{2.30}$$

Multiplying out the sums, the total Helmholtz equation is reduced to:

$$\sum_{ij} u_i v_j \int_\Omega \nabla \Phi_i \nabla \Psi_j \ \mathrm{d}\Omega - k^2 \sum_{ij} u_i v_j \int_\Omega \Phi_i \Psi_j \ \mathrm{d}\Omega \tag{2.31}$$

$$-ik \sum_{ij} u_i v_j \int_{\partial\Omega} \nabla \Phi_i \nabla \Psi_j \ \mathrm{d}\Omega = \sum_{ij} f_i v_j \int_\Omega \nabla \Phi_i \nabla \Psi_j \ \mathrm{d}\Omega \tag{2.32}$$

Because a computational model cannot handle infinite subspaces, the chosen subspace is dimensionallt finite. If the coefficients of the orthogonal bases are combined in vectors:

$$\vec{u}^T = [u_0, u_1, ..., u_N] \tag{2.33}$$

$$\vec{v}^T = [v_0, v_1, ..., v_N] \tag{2.34}$$

$$\vec{f}^T = [f_0, f_1, ..., f_N] \tag{2.35}$$

and by introducing following matrices:

$$K_{ij} = \int_{\Omega} \nabla\Phi_i \nabla\Psi_j \, \mathrm{d}\Omega \tag{2.36}$$

$$(M^{\Omega})_{ij} = \int_{\Omega} \Phi_i \Psi_j \, \mathrm{d}\Omega \tag{2.37}$$

$$(M^{\partial\Omega})_{ij} = \int_{\partial\Omega} \Phi_i \Psi_j \, \mathrm{d}\Omega \tag{2.38}$$

we can reduce 2.24 in a more compact form:

$$v^T K u - v^T M^{\Omega} u - v^T M^{\partial\Omega} u = v^T M^{\Omega} f \tag{2.39}$$

Since equation 2.39 is fullfilled for all possible values of the testfunction v, the vector u is a solution of the PDE if and only if:

$$Ku - M^{\Omega} u - M^{\partial\Omega} u = M^{\Omega} f \tag{2.40}$$

The Galerkin Method, is able to approximate the Helmholtz equation by a matrix equation, which can be handled by available linear algebra toolboxes like BLAS, or numerical programs like Matlab. The quality of the approximation is limited by the size of the linear subspace, e.g the number of discrete elements.

One remaining question is how to choose the subspace. There are two common ways in selecting the base of the subspace[41]. The first way is to use the whole domain and to find an appropriate orthonormal base of functions to describe the domain. A typical example is the approximation of a solution in Fourier components or spherical harmonics. The other way to select a basis, is to split up the space in small disjunctive elements, where the supply of the function is only defined over this element. A common example of the latter strategy is the method of Finite Differences.

The great advantage of the Galerkin method is the freedom in choosing the subspace. Finite element approaches typically utilize both strategies to

define the subspace, by breaking up the complete space in small elements, over which a small base of functions is used (constant, linear, quadratic....). As earlier mentioned Finite Differences are a sub-class of finite element methods. In finite differences (2D model) a plane is divided in rectangular elements of equal size. It is a method easy to implement, but has a draw-back. The spacing of the numerical grid over the whole domain is constant. As a consequence the computation of fields in some areas take a high amount of computational time, even if this area is not interesting for the problem. On the other hand, areas of interest may be calculated within a too coarse grid.

The simulations in this work have been calculated in a non-uniform triangulation of the domain, to achieve a high resolution in the area of interest. As finite element packages FEMLAB (now known as Comsol Multiphysics) and FreeFEM++ (under GPL) have been used. Both use Arpack and umfpack as solver for the linear systems.

The FEMLAB system was originally developed by mathworks and has a strong attachment to MATLAB. The user interface is intended for user-friendly interaction and the differential equation is directly entered in predefined templates. FreeFEM is a text-based interpreter that utilize the weak formulation of the partial differential equation.

Due to the complexity of the problem and the available computational power, all models have been reduced to two dimensions. A complete three dimensional model would result in an increase in elements from n^2 to n^3.

2.1.2 Comparison to a known system

In the following section, the simulation of waveguiding structures is described. With aim to reduce computational power, structures that are symmetric in z-direction are investigated. In case of organic nanofibers, this

approximation is reasonable, because of their extraordinary aspect ratio.

A separation ansatz in z, $\vec{E} = \tilde{E}e^{i\beta z}$ for the electrical field results in:

$$\Delta_{xy}\tilde{E}\left(-\beta^2 + \frac{n(x,y)^2}{c^2}\omega^2\right)\tilde{E} = 0 \tag{2.41}$$

$$\tag{2.42}$$

The propagation constant β, that is introduced here is correlated to the phase velocity in z-direction by $v_z = 2\pi\frac{\beta \cdot c}{\lambda}$. The influence of β on the solution is discusses at the example of a circular waveguide. A a circular waverguide consists of a core with a high index of refraction n_2 inside a circle of the radius r, surrounded by a low index of refraction material $n_1 \leq n_2$. A solution of 2.41 for this geometry depends on the value of β. The behavior of the solution can be categorized by three cases[31]:

1. $\beta\lambda \leq n_1 \leq n_2$
2. $n_1 \leq \beta\lambda \leq n_2$
3. $n_1 \leq n_2 \leq \beta\lambda$

In the first case, $\beta\lambda \leq n_1 \leq n_2$, the sign of the linear factor in 2.41 is positive in all regions. (the linear factor is $-\beta^2 + \frac{n(x,y)^2}{c^2}\omega^2$). The equation is of Helmholtz nature in the entire cross-sectional plane. The resulting electrical field has oscillating components over the whole space within the plane.

The opposite behavior can be observed for the third case ($n_1 \leq n_2 \leq \beta\lambda$). In this case the PDE is of Laplacian kind and can be approximated by an exponential function far away from the core. Since the field and its derivative have to be continuous over the boundary of the core, the exponential behavior would continue monotone inside the core region. As consequence, the electrical field would increase to infinity along a certain direction. This

solution is physically not possible under the condition, that the field stays finite.

The second case is a mixed scenario. In the core region, the equation is Helmholtz like, in the outer region, the equation behaves like a Laplace equation. A solution of this problem shows exponential behavior in the outer regions, but oscillates at the region of the core. Due to the oscillating term in the core it is possible, that the field is not longer monotone and a solution with a non-zero field inside the core exists, exponential decaying on in all directions.

The interpretation of the first case is describing the scattering of an external light wave at the core. Integration over the xy-plane shows that the amount of field energy inside the fiber is neglectable to the total field strength in the whole system. Since these fields are optical waves, that can be detected in the far field, these solution are called radiating modes

Solutions which fulfill the second case have a substantial amount of the fieldstrength confined in the core of the fiber. The exterior of the field is exponentially decaying in the evanescent wave. Because of the conservation of all the field energy at the core region, this solutions are called guided modes.

The analytical solution of the cylindrical geometry can be found by solving the Laplace equation in cylindrical coordinates. Results are Bessel and Hankel functions of the first kind[39].

To find a finite element solutions for the configuration of cylindrical waveguides wit FEM methods, we have to calculate the eigenvalues of Equation 2.39. Compared to numerical models based on Green functions, FEM models result in sparse matrices. Large scale eigenvalue solver can take advantage of the sparse form and effective algorithms for solving the problems do exist (for example Arnoldi iterator, used in the arpack package.)

Due to the fact that only guided modes are of relevance for observing wave-guiding, the propagation vectors β is limited between $n_1 \leq \beta\lambda \leq n_2$. Since the Arnoldi solver works best for small eigenvalues, it is possible to reduce numerical errors in the solution by tweaking the original differential equation. The boundary conditions applied at the borders are of Sommerfeld type, to ensure that the fields vanish at the border of the computational domain. The computational domain was chosen to be 40 times as big, as the modelled structure, with coarse triangulation around the border and refinement at the core. With boundary conditions, that require the field to vanish at the borders of the computational domain, it can be shown, that the solution of

$$\Delta\tilde{E} - \frac{n_1^2}{c^2}\omega^2\tilde{E} = 0 \tag{2.43}$$

is zero in the complete domain. Adding this to the Helmholtz equation results in

$$\Delta\tilde{E} + \left(\frac{n(x,y)^2 - n_1^2}{c^2}\omega^2 - \beta'^2\right)\tilde{E} = 0 \tag{2.44}$$

This equation produces the same solutions like 2.41, but the propagation constant is shifted to a range of $0 \leq \beta' \leq \sqrt{n_2^2 - n_1^2}$ for guided modes[23]. This model was passed to the FEMLAB solver. The solutions of the finite element model are compared in table 2.1.2 with the solutions found by analytical calculations.

2.2 Propagation in organic Nanofibers

In the last chapter a theoretical model for calculating electrical field distributions in dielectric waveguides was introduced. The model has been checked for correctness against a known system. In this chapter we are going to use

this model to predict behavior relevant to the guiding of light in organic nanofibers.

Organic nanofibers are grown on mica substrate and can be transferred to

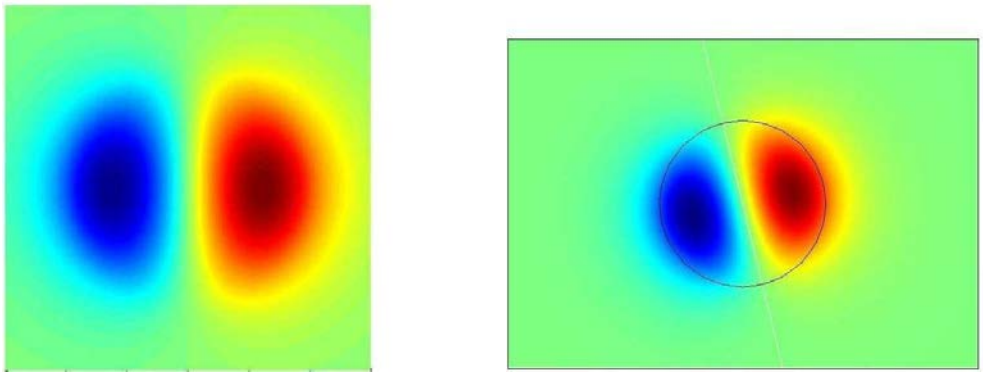

(a) (b)

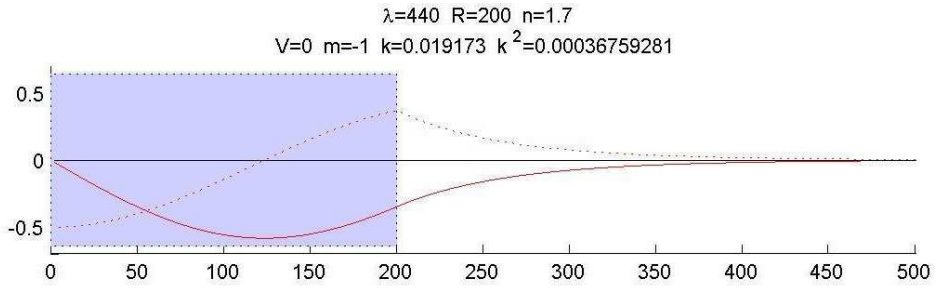

(c)

Figure 2.1: Comparison of the finite element model to a known system. Figure (a) shows the analytical calculated field distribution of a TEM_{01} mode in a circular waveguide. Figure (b) is the same solution calculated with a finite element model. The cross-section of the mode can be seen in figure (c)

Mode	FEM	Analytical
00	4.991707e-4	4.9917072e-4
01	3.675927e-4	3.6759281e-4
11	2.140077e-4	2.140081e-4

Table 2.1: Comparison between FEM and analytic solution, for $\lambda = 440nm$, $r = 200nm$, $n = 1.7$. The listed values are calculated as $k^2 - n^2 * \frac{2\pi}{\lambda}$, where k is the propagation speed of the guided mode.

an arbitrary substrate. Since the interaction of the substrate with the optical fields has a great impact on the system, the model has to be extended to a system of three different domains, namely the fiber, the substrate and the outer environment (compare figure 2.2).

A FEM model can be adapted directly to the new configuration, by remodeling the function of the index of refraction $n(x, y)$ to represent the new morphology. An adequate approximation of the needle morphology can be done, by dividing the space along the x axis in substrate and environment and model a half ellipse on top of the substrate, representing the needle.

Following the argumentation from last chapter, the solution depends on the propagation constant β

1. $n_{vac} \leq n_{substrate} \leq n_{fiber} \leq \beta\lambda$
   Similar to the previous argumentation, solutions would exponential increase and do not represent any physcal relevance.

2. $n_{vac} \leq n_{substrate} \leq \beta\lambda \leq n_{fiber}$
   Describes guided modes inside the nanofibers.

3. $n_{vac} \leq \beta\lambda \leq n_{substrate} \leq n_{fiber}$
   These modes are radiative. The solutions describes optical fields, that are total internal reflected on the interface between the substrate and air.

4. $\beta\lambda \leq n_{vac} \leq n_{substrate} \leq n_{fiber}$
   The solutions with a propagation constant in this range are optical fields refracted at the structure.

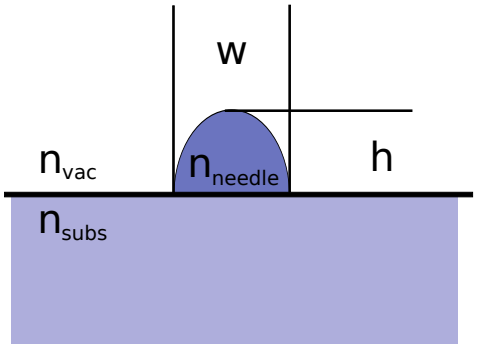

Figure 2.2: Design of the computational setup for FEM analysis. The substrate extendeds to $-\inf$. The cross-section of the needle is half of an ellipse

According to the simulation of the circular waveguide, the simulation is shifted to obtain eigenvalues between $\beta^2 - n_{subs}^2$. The triangulation has been chosen coarse on the computational domain and has been refined around the fiber. In the simulation, the width and high of the needle has been altered systematically. A change in geometry requires a new triangulation, which implies a recalculation of the stiffness matrices. These steps have a major impact on th speed of the simulation.

First the existing modes are investigated. In contrast to hollow metallic waveguides, dielectric waveguides always provide a solution of at least one guided mode and higher order modes show a distinct cut-off wavelength[18]. For wavelengths longer than the cut-off wavelength, a multi-mode propagation doe snot exist[37].

The Helmholtz equation allows a scaling of the solution, in terms that

two system behave equal, if the dimensions scale with the wavelength.

$$\Delta\tilde{E}(x,y) + \left(\frac{\omega^2 n(x,y)}{c^2} - \beta^2\right)\tilde{E}(x,y) = 0 \quad (2.45)$$

$$\Rightarrow \Delta\tilde{E}(\alpha x,\alpha y) + \left(\frac{\alpha^2\omega^2 n(\alpha x,\alpha y)}{c^2} - \alpha^2\beta^2\right)\tilde{E}(\alpha x,\alpha y) = 0 \quad (2.46)$$

The wavelength chosen for the simulation was set to 440nm, because the fluorescence emission spectrum shows a peak around this wavelength. The results of the simulation can be seen in figure 2.3.

For typical dimensions of nanofibers (width $<$ 200nm, height $<$100nm), only the fundamental mode exist. The difference between the index of refraction of the substrate to the index of refraction of the fiber is influencing this behavior. For a high difference, multi-mode propagation can be found at fiber sizes of 300nm x 300nm. By choosing a substrate with a index of refraction close to the index of refraction of the fiber material, higher modes are suppressed.

This behavior can be understood by looking at the field distribution. Solutions with a propagation constant close to the index of refration of the substrate (what is conform to be close to the cut-off wavelength), have a high amount of field-energy propagating outside the fiber. Since the difference in the index of refraction between fiber and substrate is smaller than the difference between fiber and vacuum, the evanescent field tends to leak stronger into the substrate. For a small needle the major amount of field energy is located inside the substrate.

The evanescent field in the vacuum is of interest for possible application. A future sensor principle based on organic nanofibers may consist of probing molecules attached to the surface. Fluorescence of these molecules could be excited by the evanescent field of guided modes. It is therefore desirable to have a far-extending evanescent field, enlarging the volume to be probed.

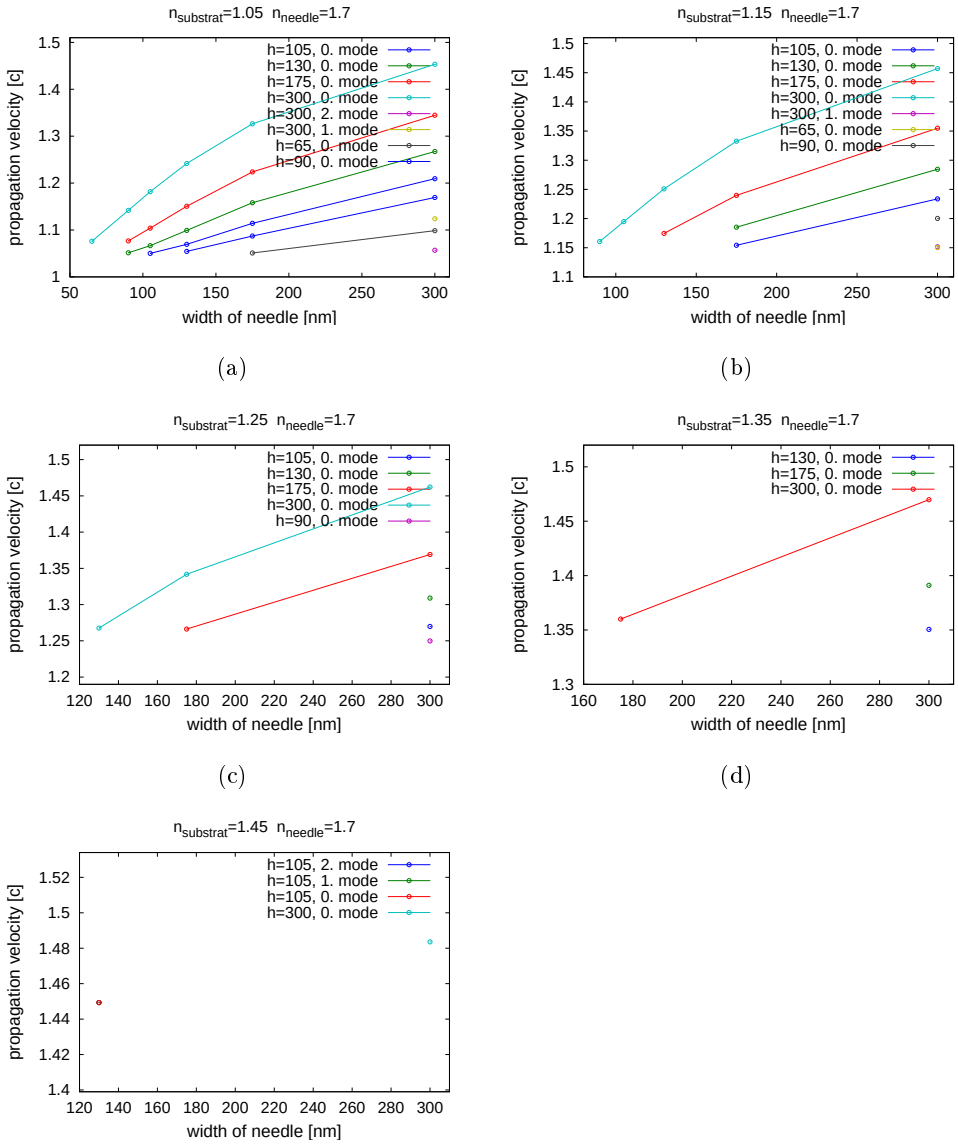

Figure 2.3: Propagation of guided modes in organic nanofibers. Figures (a), (b), (c), (d), (e) show the phase velocity in dependence of the width of the needle for different heights. The index of refraction of the substrate is changed in the figures to 1.05, 1.15, 1.25, 1.35, 1.45 respectively.

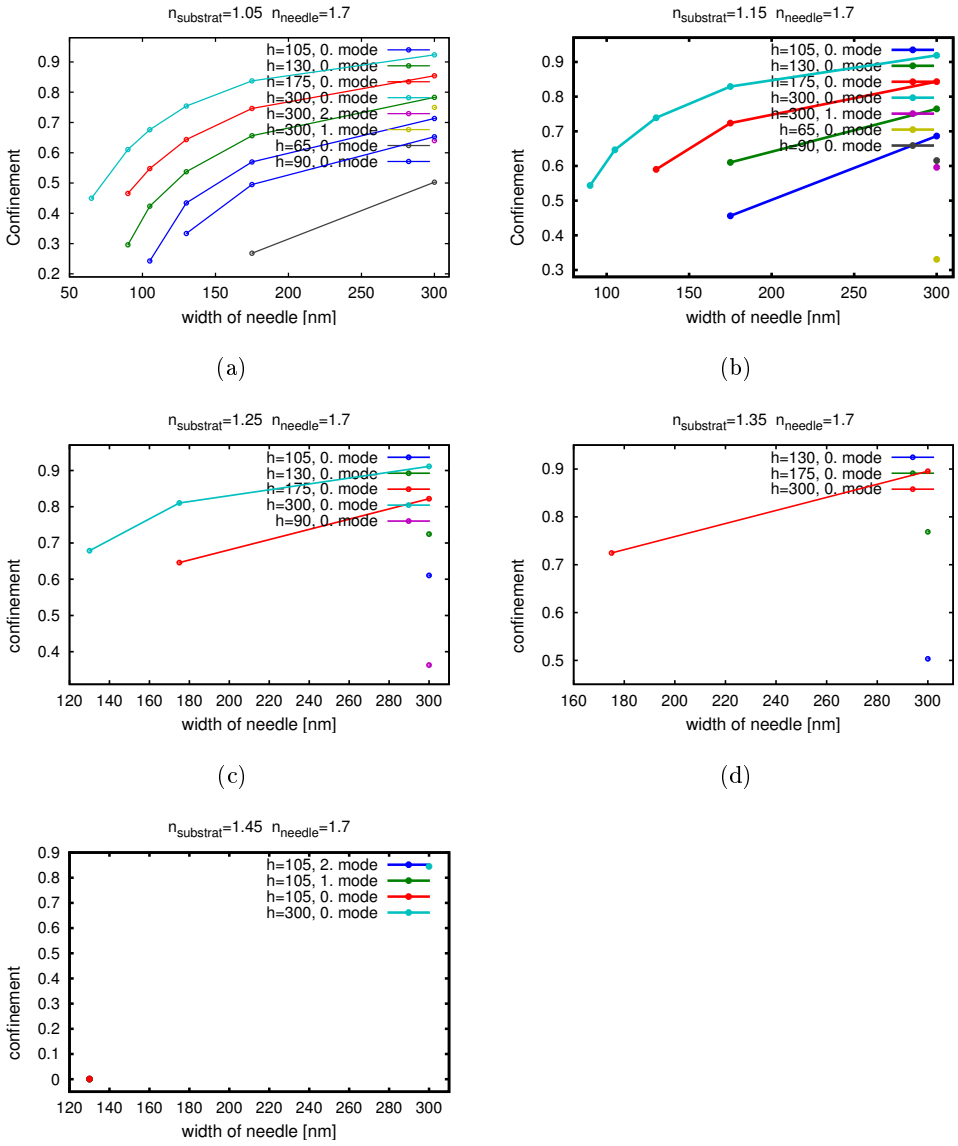

Figure 2.4: Confinement of the electrical field of guided modes inside organic nanofibers. Figures (a), (b), (c), (d), (e) show the amount of fieldenergy propagating inside the fiber. The ordinate shows the fraction of energy inside the needles normalized to a total field energy of 1.

The simulation shows, that the evanescent field at the vacuum side ha a distinct maximum depending of the width of the fiber. For higher needles,

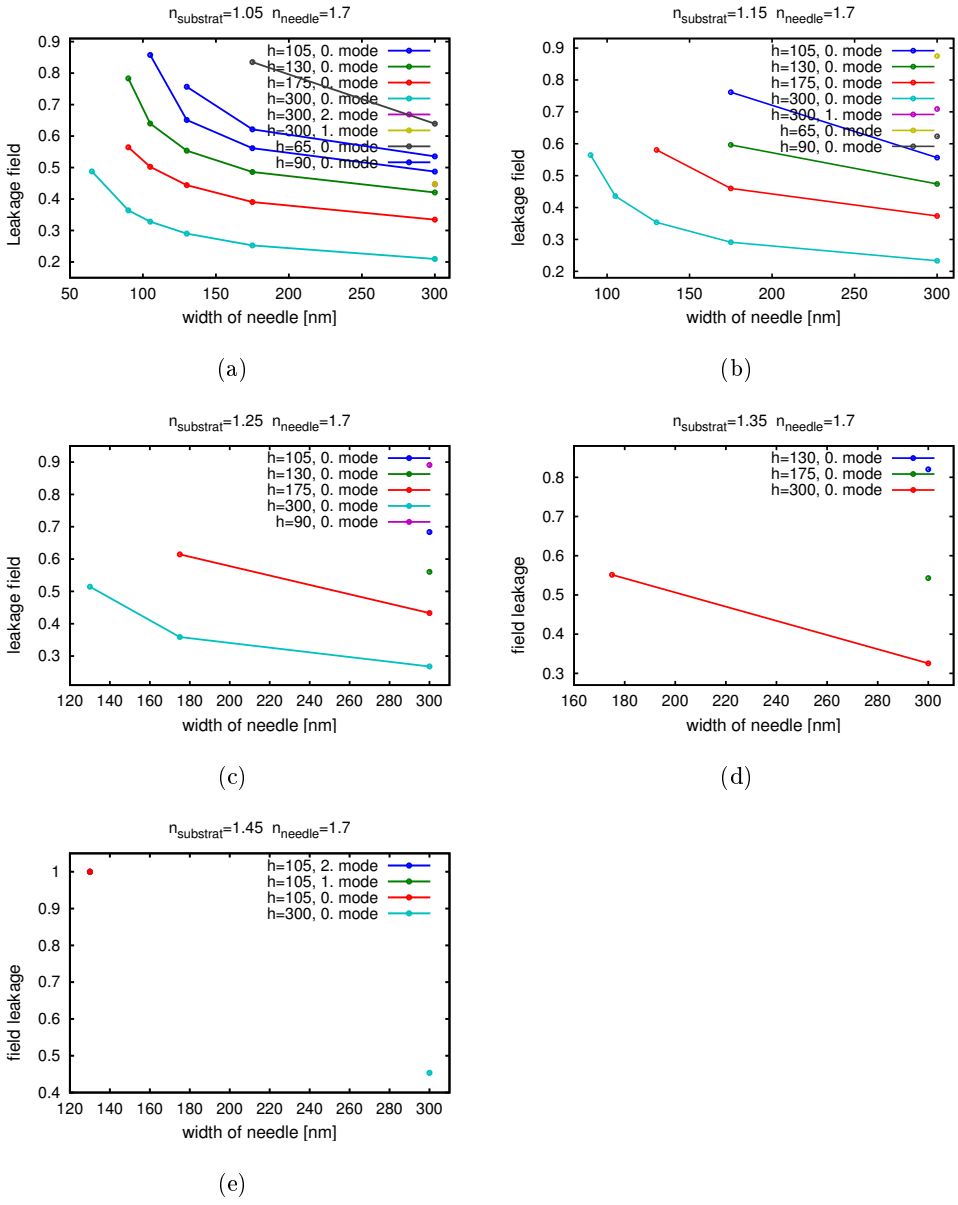

Figure 2.5: Field leakage to the substrate. Figures (a), (b), (c), (d), (e) show the amount of the electrical field propagating through the substrate in dependence of the morphology. The index of refraction of the substrate is changed in the figures to 1.05, 1.15, 1.25, 1.35, 1.45, respectively.

the center of energy of the field is located higher, exposing more of the evanescent filed on the vacuum side. If the height and width get smaller, the field is more and more drawn into the substrate which decreases the energy in the evanescent field. On the other hand by reducing the dimensions, the amount of energy confined in the evanescent field gets larger.

2.2.1 Coupling between Fibers

The simulations of fibers have shown, that a major amount of field energy is confined inside the substate. This field is located below the fiber, but can have larger dimensions, compared to the dimensions of the needle. If two distinct fibers are located close to each other, these fields will interfere. To investigate this influence, the geometry of the simulation was altered as illustrated in figure 2.2.1.

Like in the previous chapter the Helmholtz equation is solved for a geometry with two fibers. For two fibers, that are far apart from each other, the solution to one eigenvalue is degenerated. The set of eigenvectors of this solution represents an excitation of the field confined within only one fiber. If both fibers are located close together, it is possible, that the combination of both fibers are so strongly coupled, that they act as a common core (compare figure 2.2.1)

For small fibers, the common core still shows only single-mode propagation. In intermediate distances, the fibers act as separate waveguides, but the evanescent field couples both modes together. These geometries have two solutions, with different propagation constants. In the solution for the larger propagation constant, the field in the fibers is oscillating in phase (symmetric mode). The solution with lower propagation constants shows a phaseshift of π between the fields in the fibers (asymmetric mode). The symmetric solution describes also the case of two strongly coupled fibers, which only

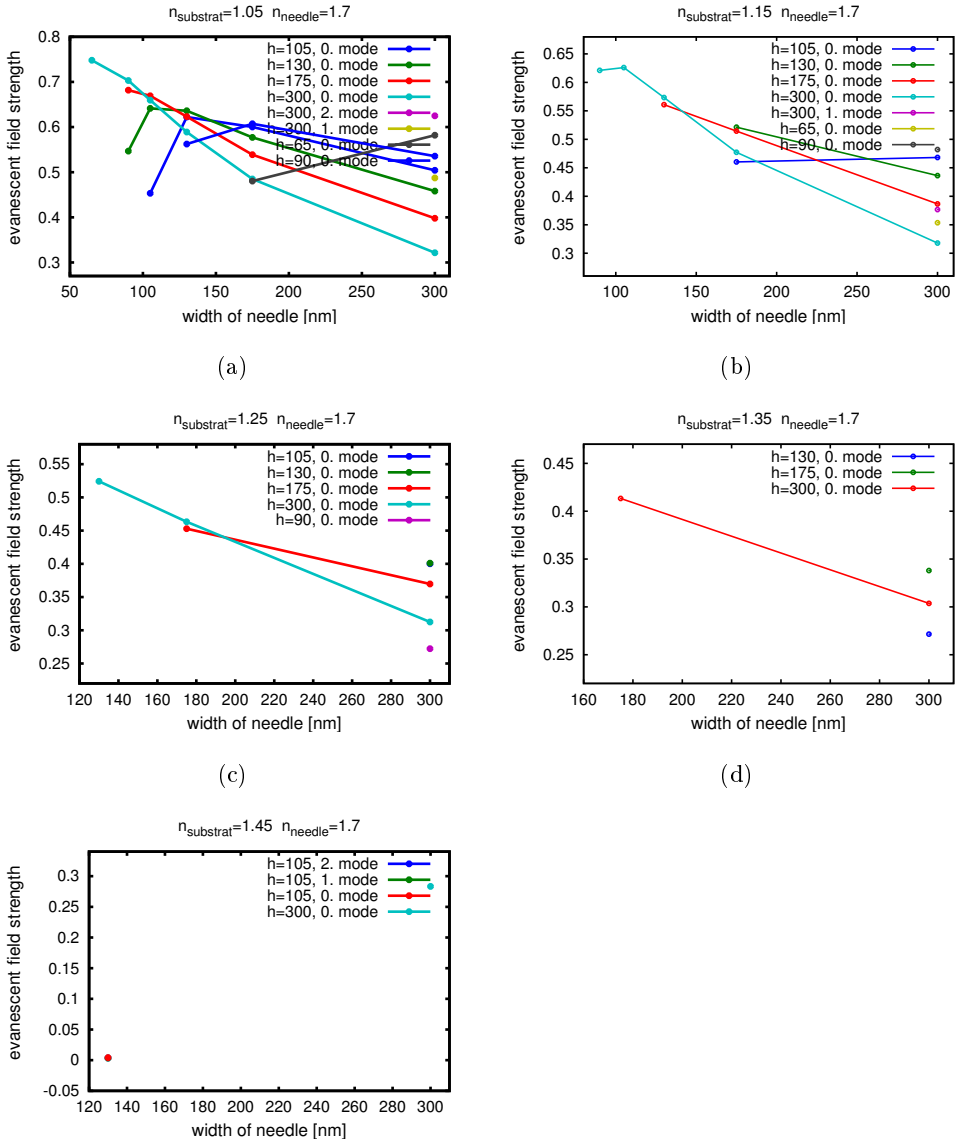

Figure 2.6: Evanescent field strength of guided modes. Figures (a), (b), (c), (d), (e) show the evanescent field strength in dependence of the morphology. The index of refraction of the substrate is changed in the figures to 1.05, 1.15, 1.25, 1.35, 1.45 respectively.

have a common guided mode.

This behavior is similar to the frequency splitting of two coupled oscillators. An excitation of light within one fiber, can be decomposed as a superposition of both solutions. During the propagation of the light field along the z-axis, both solutions propagate with different phase-velocities. After a distance of $\frac{\beta_{sym}-\beta_{assym}}{4\pi}$ the solutions have a phase difference of $\pi/2$. This does imply, that the excitation has been transferred from one fiber to the other fiber.

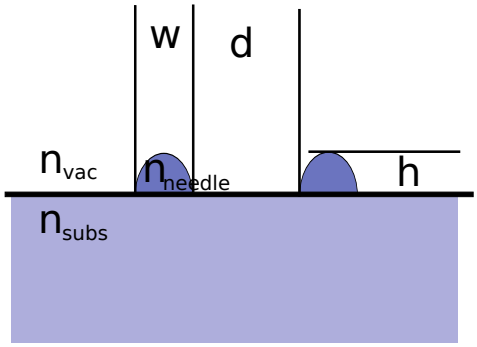

Figure 2.7: Design of the computational setup for FEM analysis. The substrate is extended to $-\inf$. The needle cross-section is half of an ellipse.

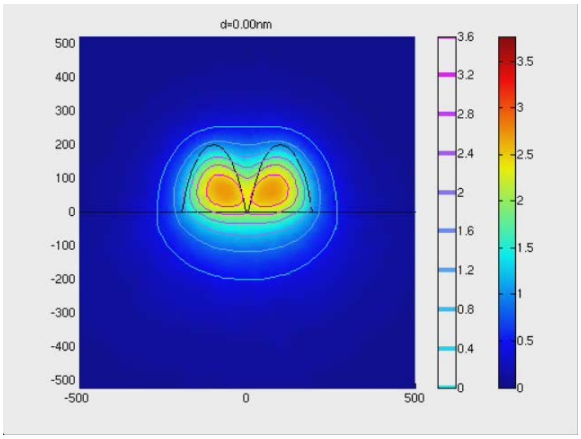

Figure 2.8: Coupling of the guided modes within two fibers.

2.3 Propagating structures

It has been shown that the field of electro-magnetic modes in dielectric structures can be calculated. One assumption made was that the cross-sectional geometry is invariant in z-direction. Organic nanofibers are up to ten thousand times longer than high, but still finite. It is of interest, how the electrical fields behave at the end of those fibers or how it is influenced by a variation along the fiber axis.

To simulate these effects, a complete three dimensional numerical model has to be made, requiring a higher amount of computational power. In this section we are investigating the effect on the propagation, but because of the mentioned requirements, the calculation is reduced to two dimensions. Therefore the structures are not anymore resembling fibers, but more the guiding of light in-between dielectric slabs.

In the previous example, we have used the propagation in z-direction to reduce the computational amount and were able to simplify the solution, by solving the eigenvalue problem. By ignoring the radiating modes, and only looking for the guided modes, the method was robust [30].

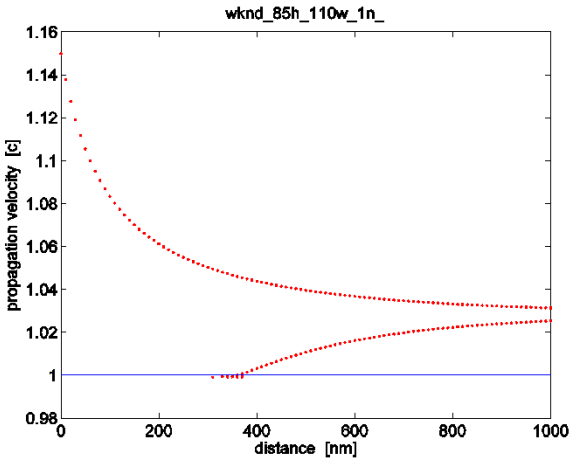

Figure 2.9: Propagation constants of two coupled fibers.

In case of propagation, the focus lies on radiating modes. In theory, the propagating setup can be also described by calculating the eigenmodes and describing the inital field, with a super-position reassembles with the excitation. This approach is not feasable, because it would require to calculate every possible eigenmode, which requires an enormous amount of computational power, and combine them to describe the correct intial fields.

The definition of boundary conditions in such a geometry is difficult, because the electro-magnetic field is a super position of the incoming and the scattered or refracted field at the boundaries. Dirichlet or Von Neumann conditions require a priori knowledge of the fields or the value of the derivative on the boundary. The incoming wave can be modeled for example by Sommerfeld boundary conditions (see equation 2.22), but a super position with the to-be-calculated scattered field sums up to different values across the boundaries.

For example, figure 2.3 shows a simulation of an diverging Gaussian beam. The divergence of the electrical field implies a curvature of the phase-planes. Fields that propagate not perpendicular to the boundaries induce reflections of the electromagnetic field. Multiple reflections and the problem of describing the field amplitudes sum up to an artificial scattered background-field.

Literature offers several kind of absorbing boundary conditions to solve this problem[12], but most of them are designed for waves coming in at a defined angle[1]. A way to overcome these limitations is to embed the computational domain into an additional absorbing layer. According to Fresnel formulas, an change in index of refraction causes a reflection of the electromagnetic fields. By matching the index of refraction of the absorbing layer to the index of refraction in the computational domain, reflections can be suppressed. This method is know therefore as 'Perfectly Matched Layer'.

Light that entered from inside the absorbing layer, is prevented from re-entering into the computational domain, by slowly increasing the imaginary part of the index of reflection, causing a smooth increase in absorption within the layer. Two implementations of altering the index of refraction are common. In the first the real part of the index of refraction is kept constant, while the imaginary part slowly increases. The second method keeps the absolute value of the index of refraction constant and slowly increases the imaginary part, while decreasing the real part of the index of refraction.

In the following simulations the latter method was used. The boundary conditions have been tested for incidence of a light beam under several angles and show sufficient absorption. The results of this investigation are plotted in figure 2.11 .

The calculations of propagating structures are more vulnerable to numerical noise and reflections from boundary conditions[27]. To examine the correctness of the simulation, it is neccesary to counter-check them in a

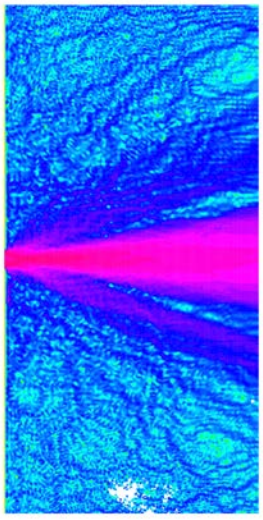

Figure 2.10: Propagation of a Gaussian beam with numerical noise due to boundary conditions

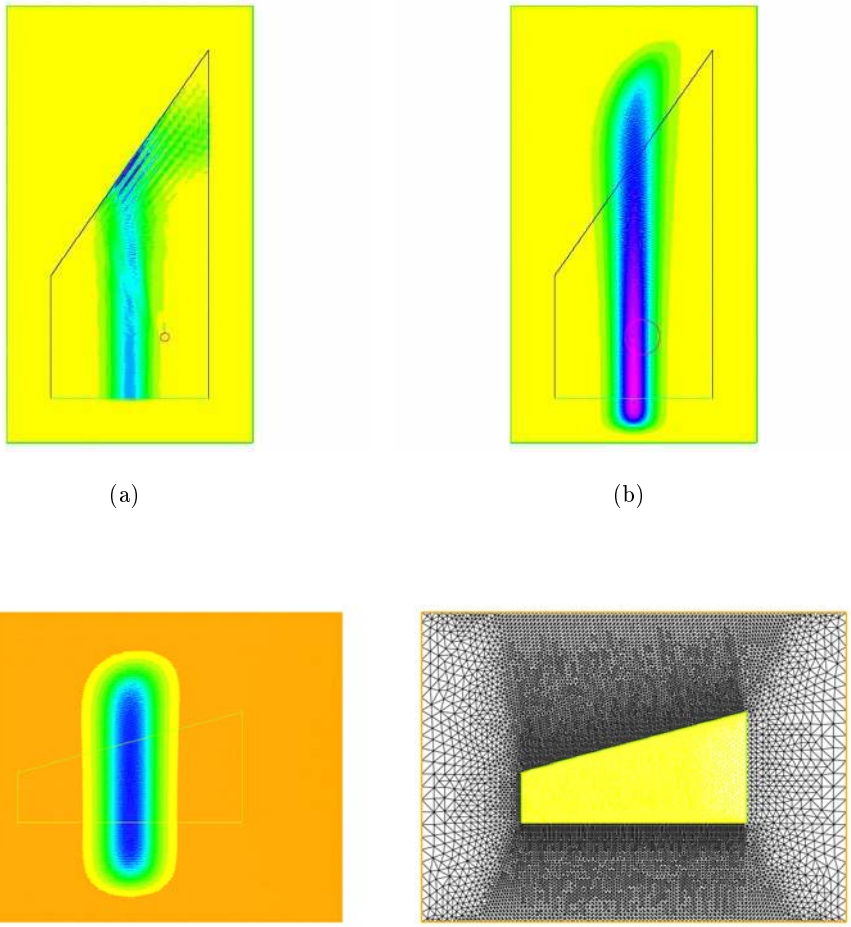

(a) (b)

(c) (d)

Figure 2.11: Figure (a) shows reflection of a Gaussian beam, launched from the bottom part of the figure. On the border of the computational domain the beam is reflected. By introducing an absorbing layer, with slowly increasing absorbing term, the reflection are minimized (figure (b)). Figure (c) shows the independence on the angle of the incident beam. In figure (d) the triangulation of the computational domain is drawn. The yellow colored region is used for calculating the field propagation, the black region is an absorbing boundary layer.

known situation. As performance standard a double slit system was chosen, where the far field pattern can be described in Fraunhofer approximation as:

$$I(\phi) = I_0 \frac{\sin\left(\frac{\pi d}{\lambda}\sin\phi\right)^2}{\left(\frac{\pi d}{\lambda}\sin\phi\right)^2} \cdot \frac{\sin\left(\frac{2\pi a}{\lambda}\sin\phi\right)^2}{\left(\frac{\pi a}{\lambda}\sin\phi\right)^2} \tag{2.47}$$

where d is the slit width and a the distance between the slits. The incoming wave was modeled as a plane wave originating from the left boundary. The simulations agree with the analytical solution in the far-field, as can be seen in figure 2.12.

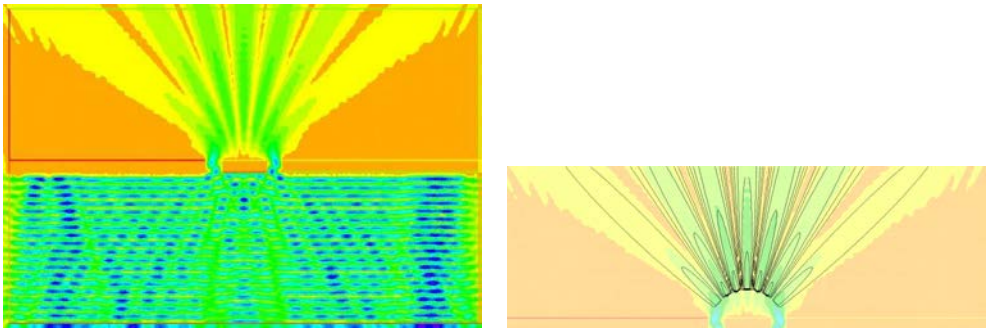

(a) (b)

Figure 2.12: Computation of double slit diffraction. Figure (a) shows a finite element simulation of the classical double slit problem. A planar wave is launched from the bottom side of the picture. In figure (b) the diffraction pattern of the FEM solution is overlaid with the contour plot of the analytical farfield solution.

To reduce numerical errors, the propagation can be remodeled, by solving for the diffence to the field distribution of an unaltered system. By extracting a planar wave propagating in +x direction from the problem, $E = u(x,y)e^{i(\omega t - k_x x)}$, the x derivatives of the Laplace equation can be formulated as

$$\frac{\partial^2}{\partial x^2}E_z = \frac{\partial}{\partial x}\left[\frac{\partial}{\partial x}\left(ue^{i(\omega t-k_x x)}\right)\right] \tag{2.48}$$

$$= \frac{\partial}{\partial x}\left[\left(\frac{\partial u}{\partial x}-ik_x u\right)e^{i(\omega t-k_0 x)}\right] \tag{2.49}$$

$$= \left(\frac{\partial^2 u}{\partial x^2}-2ik_x\frac{\partial u}{\partial x}-k_x^2 u\right)e^{i(\omega t-k_x x)} \tag{2.50}$$

and substituing the fields in the Helmholz equation results in:

$$\Delta u+(\frac{\omega^2 n^2}{c^2}-k_x^2)u-2ik_x\frac{\partial u}{\partial x}=0 \tag{2.51}$$

A promising application of futur nanofiber technolgy are devices that utilize the evanescent field of guided modes. In the previus sections, it was discussed how to influence of the cross-section of a fiber to extend the range of the evanescent field. The simulation shows the existence of an optimum geometry, which obtains a maximum evanescent field. In this section, it is tried to investigate the effect of structuring the fiber along the propagational axis, in order to enhance locally the evanescent field.

The simulations are based on the model introduced in the last section. The incoming wave was modeled to be a guided mode of the structure. Therefore the eigen-value problem for the cross-section of the propagating structure has been solved. The obtained numerical solution was fed forward in the simulation to define the incoming electromagnetic fields.

The investigated system consists of a dielectric slap structure. To expose the nearfield, a circular hole had been cut in these structures. The response of this geometry can be seen in figure 2.13.

The calculations show, that the hole squeezes the light in the area of the cut-away. For short wavelengths, the light is mainly scattered and converted to higher order modes. The numerical resolution around the cut-away region does not allow to distinguish scattered light fields from the evanescent

field. However, in the case of a simulation with a wavelength of 780nm, the electromagnetic field is also squeezed at the area of the cut-away, but at this wavelength, the structure only provides single-mode propagation. The field distribution after the hole cleans itself up to a single mode propagation, by scattering light, mainly in the direction of the substrate. A clear enhancement of the evanescent field can be observed at the entrance of the cut-way region, where the lights hits the hole.

The numerical simulations show a high amount of scattered light and numerical artefacts. To investigate if these limitations can be overcome by applying a different method of solving optical near-fields, the problem has been modeled by the differetial theory of electromagnetic gratings (DTG)[17]. Thanks to Gaëtan Lévêque, who adapted the formalism to the described structures and ran the simulation, it was possible to directly compare the results obtained by the two models (compare figure 2.14).

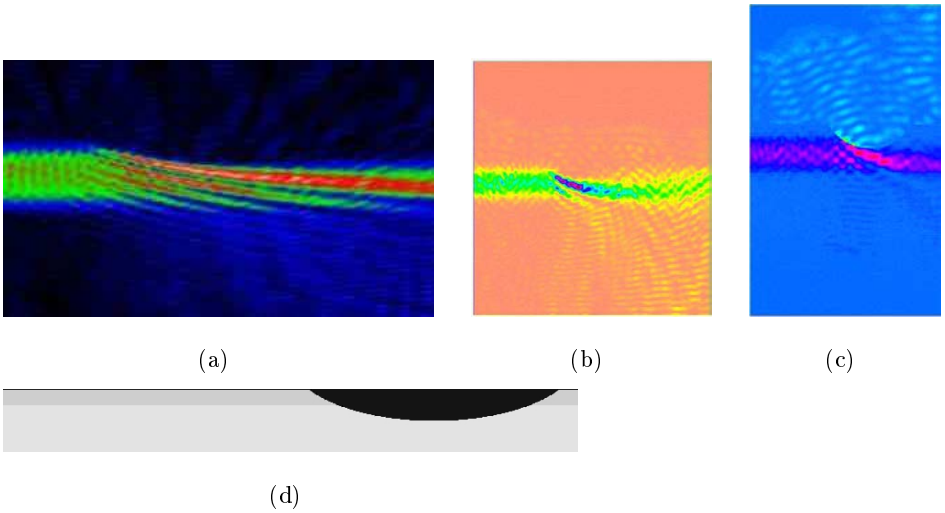

Figure 2.13: Simulation of disturbance of a guided mode in a slab waveguide as drafted in figure 2.13(d). Image 2.13(a) shows the dielectric displacement field for a wavelength of 440nm, Image 2.13(b) shows the dielectric displacement field for a wavelength of 780nm. The electric field in the latter case is showd in figure 2.13(c)

The results of both models agree in their solutions with each other. Shown DTG model is based on finding the Green function to the boundary value problem, described by the geometry [38]. This method is more robust to numerical errors compared to the FEM model, as can be seen from the graphs. The major disadvantage of the DTG method is the amount of computational power needed to solve the problem. The shown DTG simulation used eight hours on a super computer (EPFL Lausanne), while the FEM simulation had been done within two hours on a normal desktop pc.

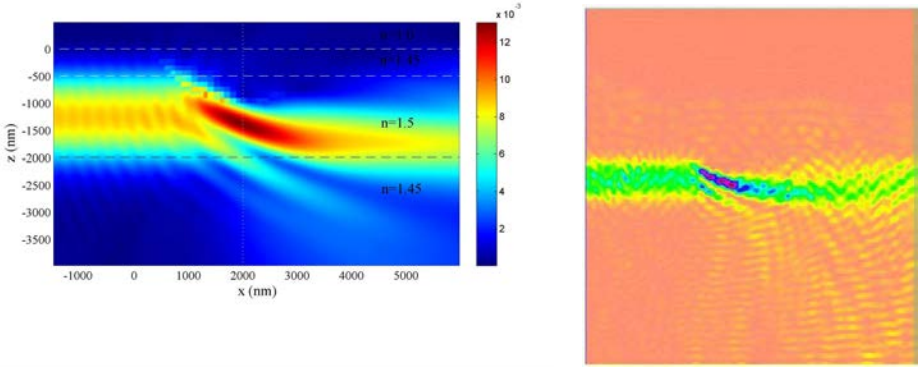

(a) (b)

Figure 2.14: Comparison between DTG method ((a)) with the according FEM model (b)

2.4 Conclusion and outlook

In this chapter a model for calculation of the near-field of sub-wavelength structures was introduced. The structures have been modeled by finite element techniques based on the Galerkin method. Inspired by the morphology of organic nanofibers, it has been demonstrated how to reduce the problem to two dimensions in the case of uniform fibers.

In difference to standard optical waveguides, the behaviour of the prop-

agation is intrinsically different, due to the absence of a cladding and the asymmetry induced the substrate. This causes that a major amount of the evanescent field is located inside the substrate.

The simulation showed, that by reducing the lateral dimensions of the structure, the amount of energy in the evanescent field can be enhanced. The amount of the evanescent field on the side of the vacuum shows a maximum for dimensions, that are typically obtained in the growth of organic nanofibers.

Furthermore it was shown, that due to the electric field within the substrate, near-by fibers are strongly coupled up to a separation distance of several times the width of a single aggregate. The weak coupling, where energy is transfered from one fiber to another, can extend over one micron.

The propagation along the fiber had been reduced to two dimensions, due to computational resources. The model for the propagation had been adapted to this case. It was shown, that the amount of reflections can be reduced by adding a perfectly matched layer[13].

Both FEM models have been verifyied against analytical solvable problems. Furthermore the method of finite elements has been compared against a model based on Green functions and the differential theory of gratings. While the latter model showed lower noise compared to the FEM simulations, the amount of computational power needed exceeded the FEM by orders of magnitudes.

The limiting factor of FEM simulations is the amount of available memory and computational power. Development on the desktop pc market show a trend to 64-bit systems, extending the limit of 4 GB of memory. Recently major graphic card manufactures are providing libraries to utilize general purpose graphic processors for numerical solving. The functionality has been demonstrated for finite element models describing fluid dynamics. Both de-

velopments show that the finite element model can be further advanced.

Recently V. Bordo has shown, that the shape of a sub-wavelength fiber can influence the far-field emission characteristics. These introduced methods can be used to compare the semi-analytical solutions with numerical calculations.

The light guiding properties of organic nanofibers have been shown for the intrinsic fluorescence. Since the fluorescent radiation is generated within the cross-section of the fiber, no coupling mechanism of light is needed. To overcome problems of re-absorption a non-resonant wavelength may be used. Coupling of light within the fiber is a major problem of this application. The presented methods can be used to find coupling mechanisms with external light fields.

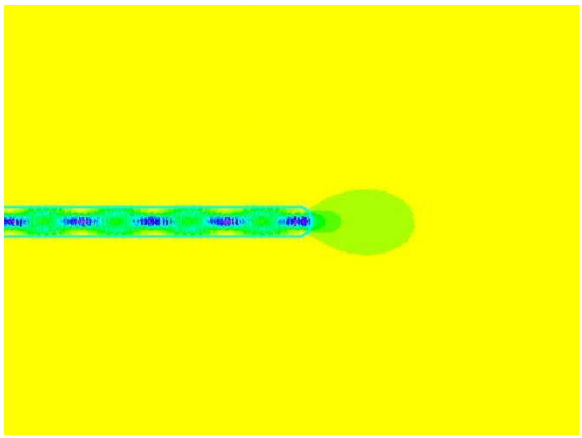

Figure 2.15: Simulation of the effect of the end shape of an sub-wavelength optical fiber on the field distribution.

Chapter 3

Manipulation of Self-Assembled Growth

The tailoring of the properties of organic nanofibers to application-specific needs is most desirable to extend the spectrum of possibilities of implementations of organic nanofibers in future devices. On the one hand, it is possible to manipulate nanofibers for a specific application after their growth. On the other hand an alteration of the growth can produce new features that are suitable for new applications.

It has been shown, that by choosing the substrate temperature and evaporation rate in the growth parameters, one can control the average length, height and width of the organic nanofibers. Additionally of controlling the growth process, it is possible to alter the growth mechanism by manipulating the substrate properties and the molecules. Both methods are demonstrated in this chapter.

3.1 Functionalization

Fiber-like aggregate formation has been demonstrated from various substances on various substrates[28]. From the variety of substrates and materials, the growth of para-n-phenylenes produces extra-ordinary aggregates in terms of alignment and uniformity. The aggregates are forming well-separated, parallel arrays over the whole surface and their length can be up to several 100 μm.

This behavior is based on a strong interaction between surface dipoles on muscovite mica and induced dipoles in the rod-like molecules, because of their dislocated Π-electron system. The lengths of the final aggregates depend on the number of phenylene rings in the molecule. Longer molecules are also forming longer aggregates.

Manuela Schieck succeeded in synthesizing functionalized para-quaterphenylene molecules[35]. By changing the molecular structure, it is possible

to influence the physical properties of these molecules, like their fluorescent spectrum or their non-linear optical response. In the following section it is described how a change of the molecular structure influences the growth of aggregates.

The investigation has been done for three different functionalized variants of para-quarter-phenylene (p4P). At the end of p4P three different endgroups had been symmetrical attached. In one series methoxy groups have been added to the ends giving a molecule of the structure MeO-p4P-MeO. The other compounds tested in the scope of this thesis has been synthesized with chlorine and with amine groups to Cl-p4P-Cl and NH_2-p4P-NH_2.

All of this substances form fiber like aggregates when evaporated under similar conditions like p6P[9, 10]. In figure 3.1 the formation of nanofibers from methoxy functionalized para-quarter-phenylens is shown.

The nanofibers, that are grown from these molecules, show new features compared to the nanofibers from p4p or p6p. Methoxy functionalized fibers change orientations in sharp kinks. From atomic force microscopy it was possible to measure the cross-sections of these nanofibers. The shape of the nanofibers is depending on the evaporated amount of material. On low nominal thicknesses of evaporated material, the cross-section of the fibers is rectangular. The upper face of the fiber is flat on a molecular level on a length scale of several μm. When a critical height of the fibers is sur-passed, the growth becomes unstable and comb-like facetting is observed like it can be seen in figure 3.1.

The other molecules also show needle growth. It is remarkable that each of the molecules has a different cross-sectional shape as can be seen in figure 3.2. It has been shown, that the width, height and length of organic nanofibers can be tuned over a certain range, by setting the growth conditions [27]. With the ability to modify the fibers from a molecular point of view it

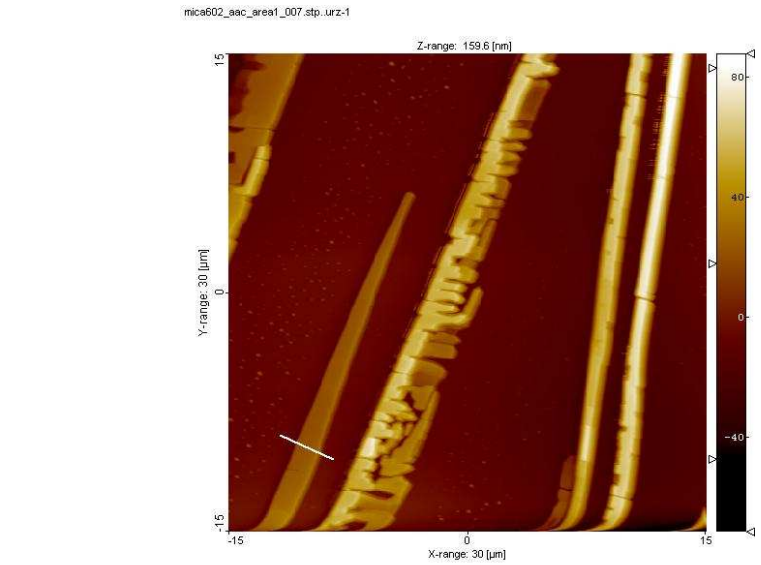

(a)

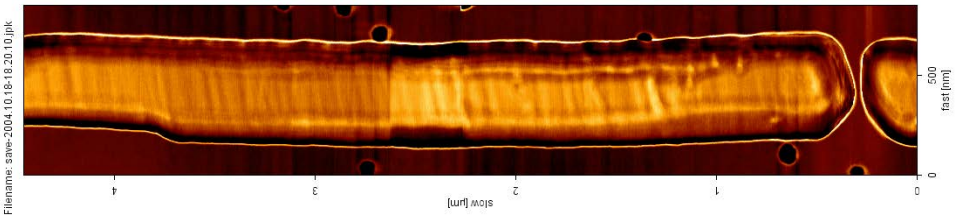

(b)

Figure 3.1: AFM images of methoxy functionalized nanofibers. Image (a) shows a false-color image of the height of the fibers. In figure (b) the phase-signal of a p6P nanofiber is drawn. The orientation of the molecules is clearly visible.

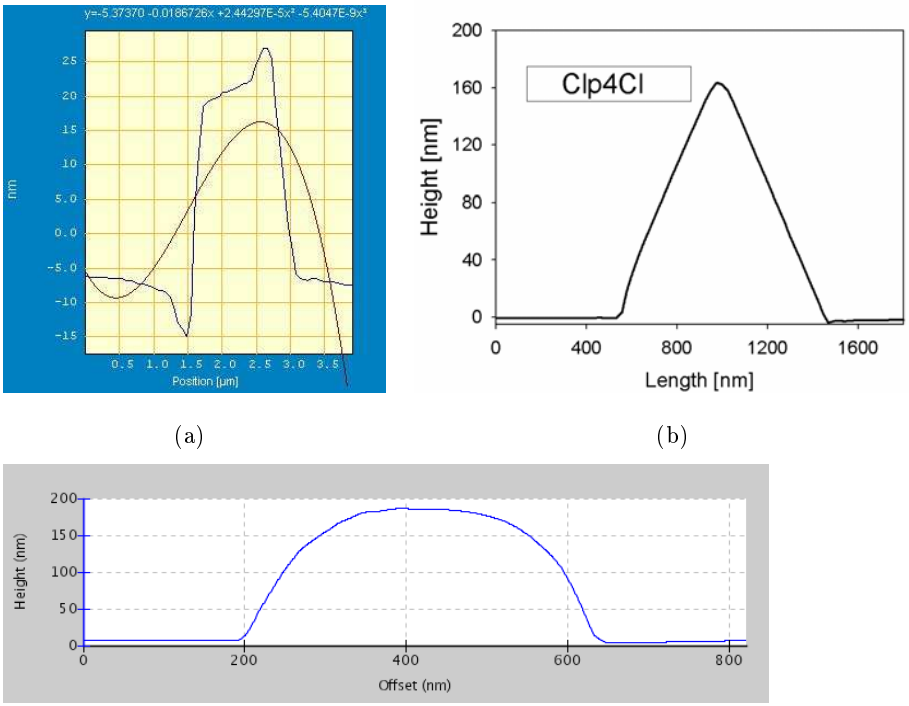

(a) (b)

(c)

Figure 3.2: Cross-section of organic nanofibers grown from different functionalized molecules. Figure (a), (b), (b) are fibers grown from MeO, Cl_2 and NH_2 functionalized para-4-quarterphenylene molecules.

is not only possible to change the optical properties with the material, but also directly influence the shape of the nanofibers.

According to the previous chapters, the performance of the waveguiding of light depends on the geometry of the cross section. By tayloring the molecules it is possible to build application-specific nanoscopic optical waveguides.

3.2 Predeposition of Gold

Another way of influencing the morphology of nanofibers is by conditioning the growth substrate[8]. This has been done by pre-deposition of gold. Freshly cleaved mica has been transferred into a vacuum chamber, where a thin layer of gold was evaporated by electron sputtering.

To ensure the same growth condition for the series, several steps of variable thickness of gold have been evaporated on the same substrate. The so prepared sample was transferred to another vacuum chamber, where the growth of para-hexa-phenylene nanofibers has been performed.

In this chamber the substrate had been heated to a temperature of 400K and been degassed for one hour. P6p was evaporated from a Knudsen cell at low evaporation rates of $0.2\frac{\text{Å}}{s}$. The deposited amount of material was equivalent to a nominal thickens of 8nm measured by a quartz microbalance.

After the samples cooled down to room temperature, they were taken out of the vaccum chamber and were analyzed by fluorescence microscopy and atomic force microscopy.

In figure 3.3 fluorescent images of nanofibers can be seen for different coverages of pre-deposited gold layers. For low coverages of gold, the overall length of nanofiber is reduced. The smallest length was observed for gold

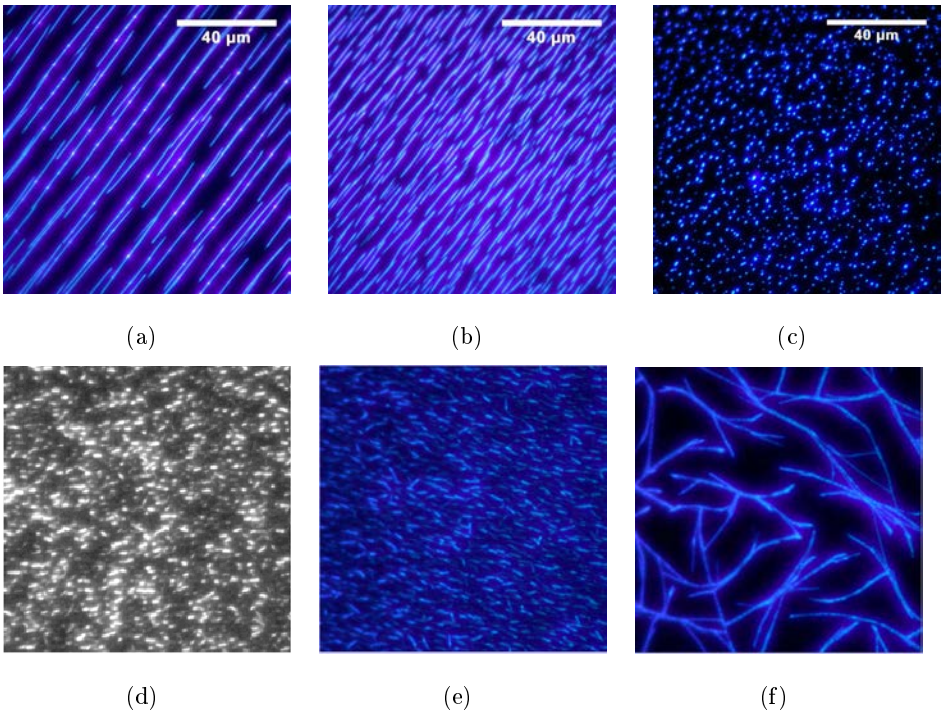

Figure 3.3: Figures , (a), (b), (c), (d), (e), (f) show the growth of organic nanofibers on muscovite mica with a pre-growth deposition of gold. The evaporated amounts of gold are 0nm, 2nm, 5nm, 8nm, 11nm and 17nm respectively.

thicknesses of 5nm. The atomic force microscopy images show, that the gold is not forming a smooth surface, but tends to cluster growth.

The growth of organic nanofibers is based on the formation of local clusters, which agglomerate to a nanofiber. The fact that the length of the fibers increases with the substrate temperature indicates, that the length of nanofibers depends on the mobility of these small clusters on the surface.

The applied gold layer increases the surface roughness and reduces the mobility of the p6p-clusters. Below 5nm, the size of the clusters does not influence the orientation of the needle growth and a preferred direction of the aggregates is visible.

Thicker coverages of gold form a closed gold film with (111) orientation. Another effect is the shielding of the surface dipole moments. The fiber length starts to increase again with increasing gold thickness, but due to the reduced influence of the surface dipole moments the alignment of the fibers is lost.

At a thickness of 17nm of gold, the evaporated p-6p is forming a net-like structure of nanofibers. Within the assembly of fibers, three preferred orientations of growth are observed, which are rotated by 120 degrees to each other. This resambles the hexagonal surface structure of the gold (111) layer.

Chapter 4

Excimer Laser Materials Treatment

In chapter 3 the generation of small structures by self-assembly has been demonstrated. In the following chapter a laser-etching method is introduced to produce structures with a spatial resolution below 1 μm. Compared to the former approach, which is a typical bottom-up technique, this method is a top-down approach.

In micro-fabrication, the production of structures consists typically of a sequence of process-steps to obtain the desired structures. A typical process sequence starts from a a clean silicon wafer. After cleaning of the wafer a layer of a photo-sensitive resist is applied to the wafer by spin- or spray-coating. An image of the structures is projected on the photoresist where it induces a polymerization process within the resist (or bond-breaking depending on resist type). After the illumination, the resist is developed and rinsed, leaving a mask of resist on the places that have not been illuminated. In the next step the silicon is etched away on the places, where the resist had been removed. The remaining resist is stripped of the substrate resulting in the structured sample.

This method is well established, but is also available for only a few materials. Most of the process steps require the use of wet-chemistry, which limits this process to materials that are inert to the used chemicals.

To overcome these limitation, a different approach is used. By utilizing a deep-UV, high-power laser it is possible to produce structures by single-shot ablation. An ArF-excimer laser is used as light source in the presented setup. It produces high intensity laser-pulses at a wavelength of 193nm, that are focused down on the substrate by imaging optics. The illuminated areas are ablated by the laser and a height-structured profile on the sample is produced. This kind of material treatment offers key-advantages compared to traditional micro-production processes, namely:

dry-etching The material is removed by laser ablation. Neither solvents,

Figure 4.1: Photography of the Excimer Laser Materials Treatment Station.

resist or acids are needed to produce the structure. This allows to process materials that would react or dissolve in water or other used chemicals.

contact-free No mechanical parts are getting in contact with the surface. This process can be repeated without any wear out of involved tools or any contamination of the surface. Also it is possible to extend the setup to work with in-situ vacuum conditions.

single-step The illumination and ablation takes place during a single process step. A further lift-off processes or any other post-treatment of the sample is not needed.

Common laser-cutting setups are based on infrared lasers (e.g. CO_2, diode-laser arrays, Nd:YAG), due to of their high output power. The ablation with these lasers is based on thermal heating, inducing high thermal stress and melting around the edges of the ablated material. A deep-UV laser with

a high photon energy (6.4eV), is able to break up bonds and reduce the thermal load. Another advantage of using UV lasers is an increased optical resolution. A Nd:YAG laser has a emission wavelength around 1.064 μm while the excimer laser has a wavelength of 193 nm. At the diffraction limit, the smallest resolveable distance is given by

$$d = 0.61\frac{\lambda}{2n\sin\alpha} = 0.61\frac{\lambda}{2NA} \tag{4.1}$$

Since the smallest imageable size is directly proportional to the wavelength,the excimer laser has a 5 times higher resolution compared to an Nd:YAG laser and 50 times higher than a CO_2 laser. With the objectives used in this setup the diffraction limited resolution is around 300nm.

4.1 Principle

The basic design of the excimer material treatment station is shown in figure 4.2. The laser beam is directed by folding mirrors to the main optical path. The first element in the optical path is a computer-controlled attenuator for tuning the intensity of the laser beam. Behind the attenuator the laser beam passes diaphragms to clip it in size, before it enters the imaging part of the setup.

By using a high quality reflective microscope objective, a mask is imaged onto the sample, which is located at the imaging plane of the objective. The mask is illuminated by the excimer laser beam, and the transmitted light pattern is projected at the image plane. This light pattern is used to ablate the material and etch the structure in the sample. A magnification factor of 15x or 25x can be chosen depending on the installed objective.

The sample is attached to a computer controlled three dimensional translational stage, that allows exact positioning of the sample and a movement

in pre-defined paths.

To gain optimum feedback, the process can be observed via an additional imaging path. Since the dielectric mirrors are transparent for white light, it is possible to use these mirrors as dichromatic filters and overlay the laser path with a white light beam.

A halogen light source was mounted behind the second folding mirror, to achieve a illumination that takes the same way as the laser beam. A CCD camera is mounted above the folding mirror next to the microscope objective to monitor the ablation process on-line. The camera's CCD chip is also in the image plane of the objective, showing a preview of the etched structure.

Due to the fact that only the mask is imaged onto the sample with the halogen light source, an additional light source is needed for illumination of the sample. Typically, the processed samples have a high surface quality and the written structures are shallow. Under these conditions it is difficult to image the sample in bright-field. Therefor a dark field ring-illumination was installed, that highlights the boundary of structures and small defects

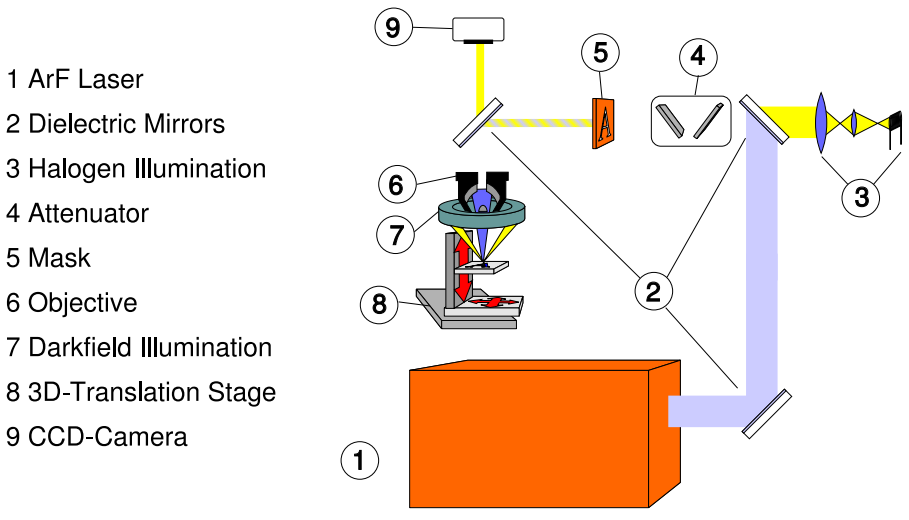

Figure 4.2: Schematically layout of the Excimer Materials Treatment Station

on the surface.

The reflective objective is free off refracting elements, that could introduce a chromatic aberration. Therefore one can be sure that if the sample and mask are simultanously in focus with white light, the image of the mask is also imaged correctly by the illumination of the 193nm light.

4.2 Experimental Setup

In order to produce defined structures by laser ablation, a high power laser source is combined with imaging and positioning systems, as illustrated in figure 4.2.

The main parts used in this setup are:

laser source : LambdaPhysik COMPex200

folding mirrors Dielectric coated mirrors from CVI

attenuator Metrolux ML2100

objective Ealing EA-25-0506 and EA-25-0514

CCD Philips CCD camera

3D-translation stage 3x Standa 8MT167-100

dark field illumination Moritex dark-field LED ring-illumination

Controller A PC with Labview programming controlling the system

4.2.1 Laser

An excimer laser is a gas laser, where the active medium is a mixture of an inert gas (Ar), halogen gas (F) and a buffer (Ne). Under normal conditions

Ar is in the ground state and fluorine is in F_2 dimer state. An electrical discharge (22kV-30kV) dissociates the Flourine molecules and excites the inert gas into its first electrical state. Argon, as a noble gas, is inert and does not form a binding. By exciting Ar* we get one electron in a s-state ($[Ne]3s^2 3p^6 \rightarrow [Ne]3s^2 3p^5 4s$). This excited electron allows argon to form a covalent binding with the fluorine atoms Ar*F. This dimer only exists during the time that Ar is in the exited state. The name excimer is itself an artifical word formed by "excited" and "dimer." Upon relaxation of the ArF compound into the ground state, Ar and F dissociate and a photon with their binding energy is emitted. The potential energy of the system Ar and F in dependence of the nucleus distance shows a repulsive behavior in the ground state at room temperature, but the first electronic state is attractive with a binding energy of 6.42 eV.

$$\mathrm{Ar^*F} \rightarrow \mathrm{Ar} + \mathrm{F} + h\nu$$

The laser used in this setup is the model COMPex 200 of LAMBDA-

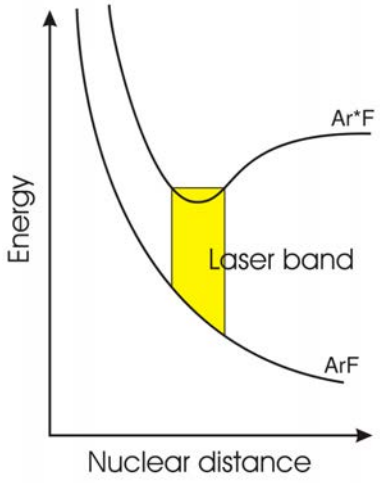

Figure 4.3: Energy of the complex of Ar and F as function of the core distances.

physics. The excitation of ArF is realized by an electric discharge in the laser tube. A capacitor array is charged by a high voltage of 22kV to 30kV, that can be triggered for discharge by a thyristor. Excimers are effective as optical gain medium. Firstly, the lifetime of the excimer is short and the influence of other decay channels is suppressed, secondly, the nuclei move apart from each other after the decay to the ground state, preventing a re-absorption of the emitted photons. Because of this, we have a high population inversion with a high optical gain. The total energy efficiency of this laser system is around 2%.

The laser only operates in pulsed mode because of the HV-discharge. The laser pulses are specified with a duration (FWHM) of 20ns and can deliver up to 400mJ of light energy. The repetition rate is limited to a maximum of 50Hz due to thermal load and because of internal replacement of the gases between two pulses.

Excimer lasers can be classified in-between classical lasers and superradiators. The output coupler of the laser has a medium reflectivity and the light is only reflected a few times inside the resonator. Therefore the beam has an inhomogeneous profile compared to other lasers, which is flatter than a TEM_{00} mode and shows fluctuations over the beam profile. In the case of material treatment, a flat beam profile has the advantage of exposing a more uniform intensity over the illuminated area. Nevertheless the fluctuations in the beam profile are for some applications too big and the beam has to be homogenized by optical components.

A disadvantage of the excimer laser, compared to other lasers, is its pulse-to-pulse stability, which is specified < 12 % and the laser gases degenerate during operation. Especially the fluorine is reacting with the tube wall and components inside the laser tube. The output power is decreasing with usage and the laser tube has to be refilled with new gas on a regular basis.

An internal microprocessor controlls the laser operation and can be accessed by a handheld terminal or R232 serial communication. Additional BNC connectors are available for external trigger and synchronization. Maintenance and basic operations are done manually by the handheld terminal.

The laser is run in high voltage mode. In this mode, the excitation voltage is kept constant, and the fluence decreases over time. This allows to access the maximum pulse energies available from the laser. Another possibility to run the system is to set the laser into constant energy mode, where the high voltage is corrected by a feedback of an internal photodiode to keep the pulse energy constant.

The laser offers a 'Charge on Demand' mode. In normal operation, the capacitors of the high voltage supply are kept charged and a trigger signal controls the discharge inside the laser tube. If the repetition rate is too low, it is possible that the capacitors self-discharge without a request, producing a laser pulse that ablates the sample at undesired places. To prevent this, the laser charges the capacitor array only when a trigger signal occurs. The induced delay (specified around 2.5 μs) is not critical for synchronization in this set-up.

4.2.2 Attenuator

The output power of the laser is adjusted by the high voltage settings and is monitored by an internal photo diode. This adjustment of the laser power is coarse and for some applications the power is still too high. A finer control of the output power is done by the attenuator ML2100 from Metrolux.

The ML2100 consists of dielectric filters and beam correction optics. The dielectric filter is designed to have low transmission loss under normal incidence and high reflectivity at a certain angle. By adjusting the angle of

incidence at the filter, the transmission can be controlled. The displacement of the laser beam by the filter is corrected by a second uncoated optics of the same thickness, aligned at the opposite angle of the filter.

The angle at the optics is controlled by a stepper motor inbetween 0 and 45 degrees in steps of 0.05 degrees. The dependence of the transmission on the angle of incidence is non-linear and has to be calibrated. The alignment of the attenuator in the beampath is sensitive and 80% of change in transmission occurs in a window of 8 degrees. A disalignment of the beam can be compensated by recording a new calibration curve.

Figure 4.4: Image of the metrolux attenuator source: metrolux product brochure.

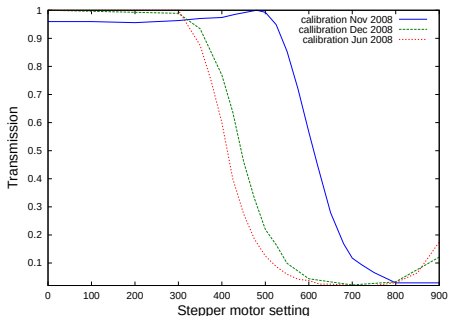

Figure 4.5: Different calibration curves after realignment. The different slope of the calibration curve from November 2006 originates form a change from p-polarized light to s-polarized light.

4.2.3 Imaging system

A challenge in designing the optical path is the wavelength of 193nm, which is at the lower end of the transmission spectrum of ambient air (oxygen strongly absorbs for wavelengths below 190nm). Usage of a lower wavelength would require either to build a setup in vacuum or a nitrogen purged environment.

The choice of materials for optics at this wavelength is limited. Metal coated optics are absorbing a non-negligible amount of light. The reflectivity of gold and silver is around 25% for 193nm light, (see figure 4.6). Applications at this wavelength use aluminum and chromium as reflective layers. Most of the standard optical glass (i.e. BK7) absorbs strongly light of this wavelength. The most common optics for the use with ArF lasers are UV-grade fused silica and MgF_2.

The high absorbance of the optics does not only reduce the power of the transmitted light, but also lowers the threshold of laser induced damages of the optics. To avoid these conflicts dielectric mirrors, that can withstand high pulse powers are used to direct the light in the setup.

The center piece of the imaging system is an objective from Ealing. The

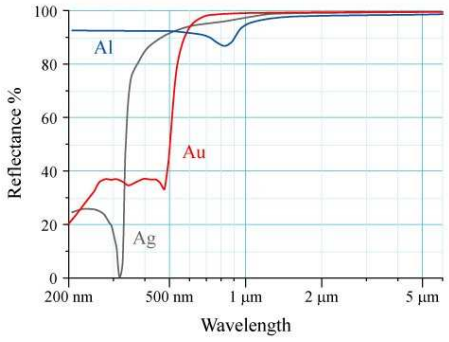

Figure 4.6: Reflectivity of common used metal coating in optics (source: Wikipedia).

objective is realized as an all-reflective objective in Cassegrain-Schwarzschild configuration. Two spherical mirrors are used, one concave, the other one convex in this configuration. The smaller mirror is attached to the housing by three legs, dividing the field of view in three segments. The outer mirror has a cut-away at the center for the entrance aperture.

This type of objective has advantages compared to refractive objectives. On the one hand the losses throug absorption are smaller, which implies that the damage threshold for the reflective objective is higher. On the other hand, the absence of refracting elements eliminates any chromatic abberation. Schwarzschild has shown, that if the two mirrors join a common center, the spherical, coma and astigmatism contribution to the Seidel abberation are eliminated, increasing the quality of the image.

A drawback is, that the small convex mirror blocks a part of the beam-path. During imaging the substrate, the center disc and the holding legs are not visible, but in the ablation process, where the objective is illuminated with a parallel laser beam, the obscuring parts prohibit the ablation to take place in their shadow.

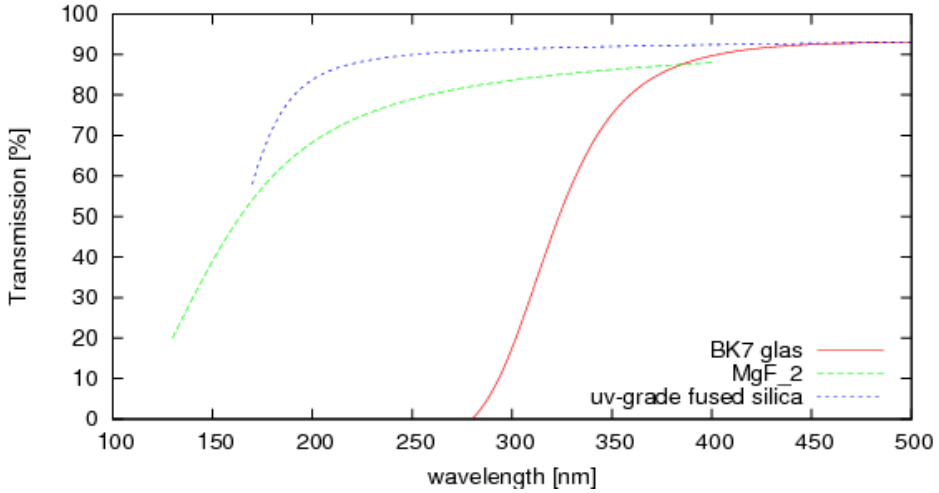

Figure 4.7: Transmitivity of optical grade materials (source: Wikipedia)

To handle this limitation, only one segment of the objective is used(in-between two holding legs, the center disc and the outer boundary) and the objective is slightly tilted. The tilt of the objective enlarges the projected area of one segment, but induces at the same time imaging errors. A trade of between imaging quality and processable area has to be made depending on the requirements of the particular application. The used 15x objective has an usable area of roughly 100μm times 100μm. The effective usable numerical aperrature is reduced by using only a segment, due to the fact that the boundaries act as a reduced aperture.

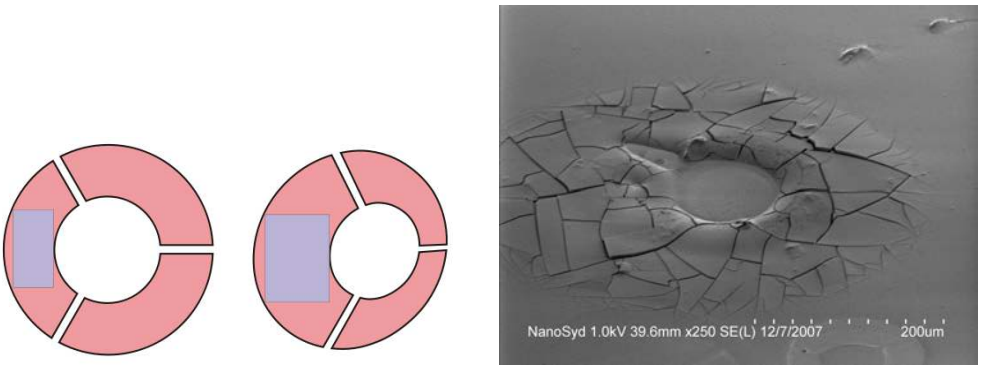

(a) (b)

Figure 4.8: Figure (a) - The inner mirror and its attachment are obscuring the beam path in the objective. In processing only the red colored part will be illuminated. The blue area shows the maximal rectangular processable area to be not affected by the obscuration. The size of this area can be increased from perpendicular illumination (left) to a tilted configuration(right). Figure (b) shows a picture of the ablated area of a complete illuminated objective. In the middle ablaion on organic meterial (pencil color) can bee seen. On the lower right side, the imprint of the objective on glas is visible with the obscured areas.

The obscured part of the objective does also effect the imaging performance of the objective, which can be best expressed with the modulation transfer function (MTF). The MTF describes the transmitted amount of a sinusoidal pattern with spatial repetition frequency k_x through the objec-

tive. Often it is visualized on the image of a black-and-white line pattern. For a large linewidth ($d \gg \frac{\lambda}{NA}$, where d is the line spacing) the pattern is imaged with nearly no distortion, and the contrast between the black and white stripes is 1. The contrast is defined as:

$$c = \frac{I_{max} - I_{min}}{I_{max} + I_{min}} \tag{4.2}$$

While the linewidth approaches the diffraction limit, the image of the bars smear out and the contrast decreases. For linewidth below the diffraction limit, where the MTF is 0, no separate bars can be identified anymore. This behavior is simulated in picture **??**. A good quality refractive objective has a modulation transfer function close to a line, starting at 1 and passing zero at $\frac{2NA}{\lambda}$.

It can be shown, that a lens itself acts as a spatial Fourier transformator, where the Fourier transform of an object can be found at the location d_f, which satisfies the following condition:

$$\frac{1}{d_f} + \frac{1}{d_s} = \frac{1}{f} \tag{4.3}$$

where d_s is the distance of the light source from the lens and f is the focal length of the lens. In the case of the Schwarzschild objective, the smaller convex mirror is located close to the focus of the bigger concave mirror and blocks the centerpart of the optical path. This influences the MTF by attenuating the lower spatial frequencies. In consequence the contrast of a reflective objective is reduced compared to a refractive objective, while simultaneously enhancing edges and small features.

While using a standard light source this effect is minor, since light is entering the objective under all angles. In the case of illumination by a laser, this effect becomes more visible. The direct laser beam illuminates the entrance apperture of the objective with a parallel beam. As shown in figure 4.8 the obscuration in the beam path is visible in the projection. In the blacked-out center, the direct laser light is blocked. Nevertheless diffracted

parts of the beam are able to enter the objective under a different angle and can circumvent the obscuring part. Since these beams are generated by the edges of the structures, a dark-field like image of the mask can be produced in the center of the objective. It is possible to produce structures at the diffraction limit by this imaging. However, the available power in this region is strongly reduced, because the major amount of energy is transported in the blocked out part of the beam.

The other use of the objective is to give on-line feedback of the process. This can be done by using the dielectric mirros as dichromatic filters, that are transparent for visible light. A CCD camera is recording the image of the sample from above. Normal samples have a high surface quality and are barely visible in white light microscopy. To enhance surface features, the

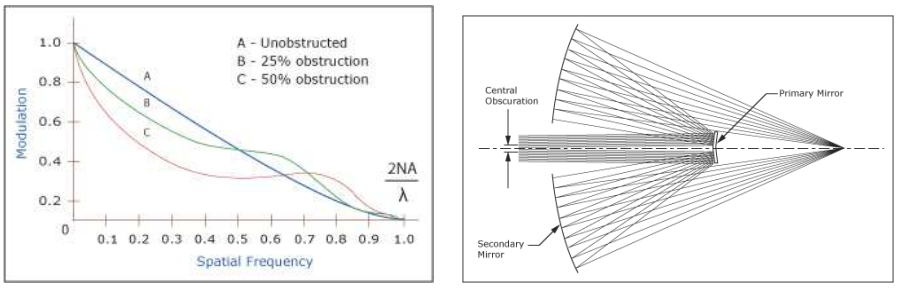

(a) (b)

Figure 4.9: Modular transfer function and beam-path of a Schwarzschild objective. The modular transferfunction is the calculation for a competetive objective (source JPS lasers.)

(a) (b) (c)

Figure 4.10: Simulation of different mode transfer functions of an objective.

sample is illuminated by a dark-field LED ring. The light originating from this source illuminates the sample at a higher angle than the numerical aperture. The direct reflected beam is not entering the aperture of the objective. Only higher order diffracted parts are imaged through the objective and give a dark-field image of the surface.

For an alignment of the mask, a halogen lamp was installed behind one of the folding mirrors. A telescope bundles the light into a beam at the same optical path of the excimer laser beam. This illumination allows to image the mask on the sample before processing and to adjust the focus and position of the image on the sample.

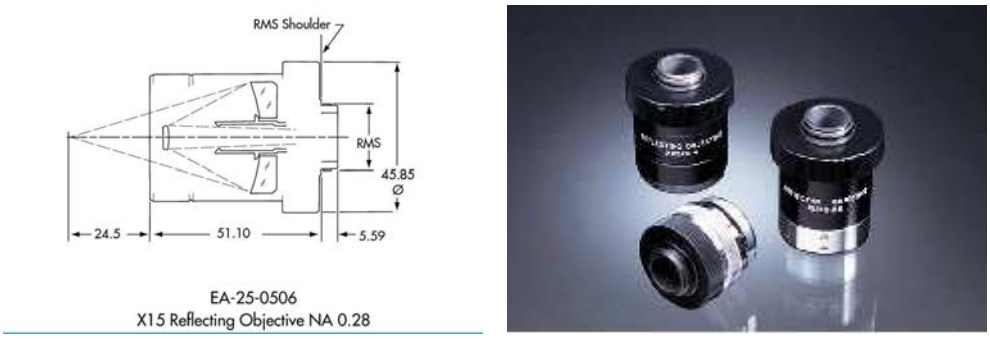

(a) (b)

Figure 4.11: Construction of the Objective. Figure (a) shows the drawing of the objective. Figure (b) shows an image of the used objective. (source: Ealing catalogue)

4.2.4 Stage

To position the sample, three motorized translational stages were combined to support a complete 3D movement. The used stages are of the model 8MT167-100 from Standa. They offer 100mm travel range with a resolution of 1μm per step. The stages are controlled by Standa's 8SMCI-USB stepper motor controller, which can control up to four stepper motors.

The controller is able to apply $\frac{1}{2}$ and $\frac{1}{4}$ steps increasing the unidirectional resolution of 250nm. The reproducibility of the stage has been tested after installing in the setup. With help of the camera and the objective the location of distinct particles could be identified with a precision of better than 1μm. The stages were able to return to the position after travel of distances of 2mm away and back (approaching the destination from the same side). The stages had a hysteresis of 7μm, which increased to more than 30μm over time for one stage. The reason for this aging was a wear out of the connector of the baseplate to the spindle. After refurbishment of all stages they show now a hysteresis below 2μm at the cost of a reduced maximum travel speed.

The stepper motor controller can be controlled over a USB 1.0 interface. An internal counter is used for storing the position. By holding currents on the coils, the stepper motor can increase the position by 1/4th of a step which would correspond to travel distance of 250nm with the used translation stages. The speed of the motor is controlled by an internal clock of 1MHz. After a user-defined amount of clockcycles, the stepper motor is increased by a fraction of a step, (selectable from 1/.5/.25/.125 of a step). The amount of waited clock cycles has to be smaller than $2^{16} = 65536$, which limits the available speeds inbetween 2 steps/s to 500 steps/s.

If two stages should move on a diagonal line, the ratio of their speeds must be the same as the ratio of the traveled distance on each axis. This ratio cannot always been set correctly because of the discretization of the

Figure 4.12: Used model of the stage.

velocities described above. In such cases, the movement of the stages has to be controlled by the software.

Software specifications

The software was designed specifically for the excimer station. The main tasks that the software has to handle are

- Manually position the stage
- Visual feedback of the Substrate
- Calibrated setting of the Attenuator
- Exposure with a defined amount of laser-shots
- Expose arrays of imaged structures
- Produce complex structures on the surface

As choice for the programming language several candidates have been considered, namely: C++, java and Labview. All three programming languages are able to produce a program in accordance with the aims. To make a choice three pre-test have been done to decide on the final implementation. The pre-test subjected interfacing the translational stages with the aim to estimate:

- implementation time
- hardware compatibility
- robustness
- features

In terms of hardware communication Labview offered the best support. All devices had been delivered with communication libraries for Labview and sufficient documentation. In C++ most of the manufacturer offered API and linked libraries for their products. For the existing camera and video card little or no information was available on how to access the hardware. In principle java offers the same functionality on communication of hardware as to C++, but requires a rewriting of the API with help of the 'Java Native Interface'. This implements an additional layer of abstraction.

The main difference between Labview and the other programming languages is it's graphical approach of 'coding', which is orientated on electrical schematics. Labview encourages the user to break up the program in as small parts as possible, because of the readability of the program. For example a class in an object orientated language can easily have a long list of object properties and methods, while in Labview a typical VI only offers up to 12 connectors for all input and output. The integrated run-time and development environment is very strict in terms of type-casts and consistency. Compared to C++ and java this makes the development of Labview executables more robust, but restricts also the functionality, like overloading of functions or type-casting (Since version 8, Labview introduced new features that allow more object-oriented design). Java and C++ offer more freedom on the realization of a problem.

Labview is a proprietary software solution by National Instruments and language definitions are decided by the manufacturer. Occurring errors can be based on software errors and are only fixed in future releases. Java and C++ have open-source compilers and a big community. For upcoming problems there is a good chance that developed free-accessable solutions exist. Labview is delivered with a library of functions covering most areas of instrumentation. Further access to hardware can be gained by communication and implementation of low-level protocols.

After the pre-test Labview had been chosen for the final implementation. The biggest impact on this decision had been the amount of time needed of implement a solution. Compared to java and c++ Labview handles redudant programming issues, for example graphics rendering or memory management. This limits the access on some components, but allows to shift focus on more relevant tasks. Comparison of the times for programming of the pre-test in the three different languages shows that development in Labview gave faster results than the other languages. While it took only two days to realize the test with Labview, the java implementation took one week, where roughly two days had been spent on interfacing the native dll, one day basic program layout, and two further days for the definition of the graphical user environment. The c++ realization has been canceled after one week, leaving a functional program, but no graphical interface. It is to mention that this had been mainly because the limited developing background with window tool-kits. The knowledge of the API-definitions for controlling the stages was already available from the previous implementation in java

Another reason for the decision for Labview was that every instrument was Labview compatible out of the box. Since the software development was done by a single person, the priority had been set on a fast development progress. In case that more developers had been engaged in this project, the decision would probably be made for one of the other languages.

design

The implementation has been done by splitting the problems up in two separate tasks. One task handles the communication with the hardware (beside the camera) the other program is for user interaction (including camera). There are several advantages taking this approach:

- Virtualization of the hardware

- Better synchronization of devices
- Mantainability/extendability
- Better control of task priorities

The user interface was designed to give easy access to the most common features of the program. The main panel displays the on-line video image for visual feed-back. Another panel offers controls for manual movement of the stage, changing the attenuation and manually triggering the laser and an abort button to stop all hardware action. An optional panel allows to control programmatic movement of the stage. A local coordinate system can be defined by moving the stage to visual alignment points. The local coordinate system is then used to map saved structures to the position of a sample on the stage. It offers possibilities to import and export GDSII data files and other formats. During the writing process of a loaded structure, the user interface is locked, except of the video signal and a button for abortion.

All actions are piped from the user interface to the hardware task. The hardware monitor listens in a separate loop with high priority for incoming commands. The main reason for using a separate task for hardware control was to prevent resource conflicts during operation. Each resource access was locked by a semaphore during an operation.

The hardware monitor was programmed as event-triggered state machine. This was necessary to handle independent operation of each sub-system. In a first attempt, each part of the hardware was controlled in a separate loop with inter-loop communication. This approach offered a cleaner software design, but due to latency and synchronization problems, this design was discarded.

Synchronization

One of the main challenges in controlling the setup was the synchronization between the stages and the laser and the attenuator. For applying a single shot, synchronization is not critical, because the laser can be triggered after the position is reached and the intensity is set. While using the laser to ablate lines and areas it is more feasible to let the laser run with a high repetition rate and move the sample synchronized. For example the drafting of a line of 1mm with a 20 x 20 μm^2 big illuminated area would take 50 shots to produce the line. The data transfer for positioning the equipment and shooting the laser lasts 300ms per instruction. The duration until the line is finished sums up to a total of 15s. With a synchronized movement to the laser the same line can be produced within 2s. If the optical stencil is 5μm$x5\mu$m big the times scale to 60s and 4s respectively.

In the first version of the controll software, a typical software action

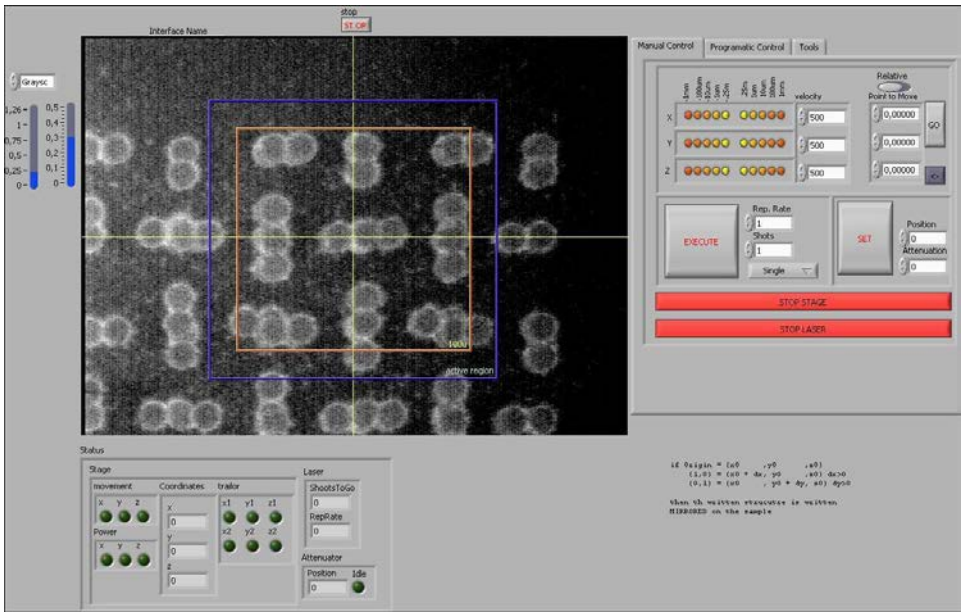

Figure 4.13: Layout of the user intereface of the ELMS software.

would consist of

- Setting the position of the attenuator
- Polling the attenuator status
- Setting the operational mode of each stage (speed, travel distance)
- Starting the movement of each stage
- Start laser loop
- Poll stage position and trigger laser until the movement finished

Two problems have to be taken into account. First, the speed of the stepper motor is discrete and has upper and lower limits. Second, the execution time of some commands are quite high and bring the laser and the movement out of syncronization.

The measured latencies of the attached devices differ by the used commands. The highest execution time was measured while communicating to the controller for the attenuator. The controller itself is connected via USB, but it simulates an RS-232 port with a bitrate of 19200. After sending a command request it can take over 50ms until the read-buffer is filled and the response can be processed. The stepper motor controllers for the linear translation stages are connected via USB 1.0. The underlying drivers and VIs are in normal operation reacting on a time span below 5ms. The setting of the operational mode, the starting of the device and the readout of the status has to be done for each axis. At the beginning the laser was controlled by setting the first data bit of the parallel port to high. The execution was below 1ms, but an additional delay of 2ms have been added before resetting the bit to ensure the trigger event. While processing the laser with a repetion rate of 20 Hz, a delay of 50ms is resulting in an offset of one shot.

The problem of the limited speed of the stage is strongly noticeable in the case of diagonals with a small angle to the axis of a stage. That means one stage is driving a long distance, another stage is only moved a short distance. To produce a straight line, the speed of the short travelling stage has to be set to

$$v_{slow} = \frac{\Delta x_{slow}}{\Delta x_{fast}} v_{fast} \tag{4.4}$$

which can sample below the lower speed limit. The resulting line would start with a steeper slope than specified (because the lower speed limit is higher) and continue in a straight line after the slow axis reached its destination.

The first steps taken to fix the timing issues were to set the fluence over one line to a constant value, because the attenuator is the slowest reacting component in this system. The non-linearity of the attenuator would require a high amount of communication with the controller to balance it to a linear slope. A feedback loop has been programmed to compensate for drifts in the stages. In the design of the feedback loop, several alternatives have been elaborated:

- **Proportional feed-back control based on time** The difference between the start-time and the current execution time of the control loop is used to predict the target position of the stages. The velocities were altered proportional to the error between the actual and target positions acording to

  $$v_{new} = v_t + \alpha_v(v_0(t - t0) - x_t) \tag{4.5}$$

  where α is the proportional gain. This compensates the timing problem that occured at diagonal lines. The timing of the stages starts earlier than the reaction of the laser. An inital offset of laser and stage is corrected by this feedback, but the spacing of the shots at the beginning of the line is closer than later distances, after the system has stabilized.

- **PI control based on time** To shorten the time until a constant movement is achieved, an additional integral part for the feedback had been added. The integral gain made it possible to correct the movement within a time periode of less than 5 loops, but the first five shots in a line were strongly displaced.

- **laser frequency adjustment based on mean position** A further improvement was done by calculating the process time of the stages based on their positions. The process time is the time that an ideal stage would have with the lowest error to the actual position of the stage. The velocity of individual stages were corrected with the previous PI loop, where the laser execution was delayed according to the next time step. This method improved the adoption to the desired position after the first shot. A new problem was that the delays accumulate and slow-down the process. A line with 100 shots had a slow-down of about 15%

The feedback loop improved the linearity and synchronization to a great extend. Two problems remained. First, the starting point was sometimes omitted because of thread scheduling. Second, the synchronization of the first point and the alignment in a line was far off.

In the beginning, the laser, stage and attenuator were treated as separate units and in some applications only the functionality of one component is needed at a time. The first layout of the steering software respected this by launching three separate threads which were specialized on controlling the different parts. A control loop gathered information about the thread status. Inter thread communication was realized by notifiers, access errors had been prevented by locking sensible resources with semaphores. Due to issues with Labview version 7, this produced a memory leak, that terminated the program after 4 hours operation with a crash.

Due to task scheduling, the laser source control loop changed it's status to processing after the stage thread completed one cycle. In consequence, the beginning of the line was not produced of the sample. By utilizing Labviews rendezvous functionality, this problem could be handled, but became obsolete with a redesign of the underlying layout to resolve the still existing problem of start synchronization.

The built-in stepper motor controller is able to control four independent axes. The controler consists of four identical PCBs, with internal connectors for synchronization. The synchronization of the cards does not simplify the synchronization during the movement, but allows to synchronize the start of each axis on a common external trigger signal. Since the fourth axis controller was unused, it was reconfigured to send a synchronization pulse out each 100 steps to trigger the laser. The start was synchronized with all four PCB by connecting them to a parallel port of the computer.

Since this fused the control loop of the stepper motor with the laser control loop, the whole hardware backend was redesigned in a single loop state-machine. A further change consisted in replacing the communication by notifiers with a command queue and the status of the hardware was stored in a global variable, realized by a non-initialized VI.

The accuracy of the stage was tested with the test pattern shown in figure 4.14(a). It consists of several parts. The first group of lines on the left side has been used to check the accuracy of points made shot-by-shot to a line with synchronized movement. The second group checked for unidirectional reproducibility. From the L-shaped group hysteresis of the axis can be determined.The last three fields check against small angle derivation, multidirectional accuracy and a vibration test.

Structure generation

To produce complex structures, the user interface was designed to send a series of commands to the hardware controller. To position the structure correctly on the sample, the local coordinates have to be correctly mapped to the stage coordinates. This was realized by three-point UV-mapping, where the user set three points on the sample to define the origin and orientation of the local coordinate system. A tilt in the sample was corrected by first degree slope interpolation.

A process of structure generation would normally involve the tracing of a path and rastering of areas. This is also in the scope of normal vector graphics, but two special features are desirable for use with the excimer laser. Information of the luminescence, or attenuation should be able to be submitted. Also an additional offset from the focal plane is of interest. To include these features a simple scripting language was implemented to control

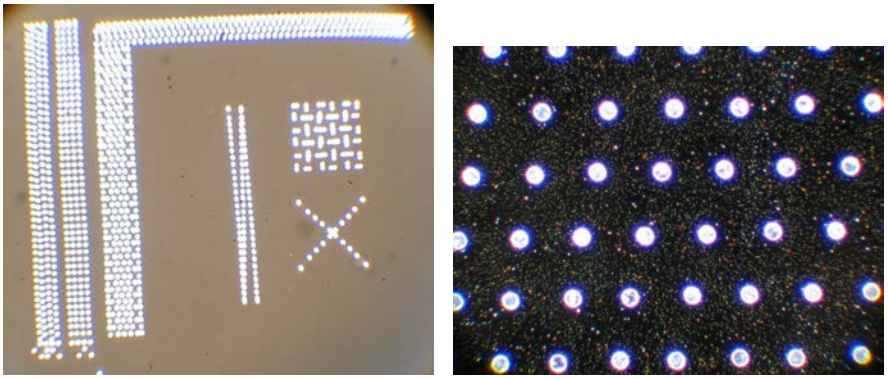

(a) (b)

Figure 4.14: The test-pattern shown in figure (a) was used to check the accuracy of the stage. This test-pattern was made with the feedback loop integrated, i.e. in the second line group from left, a speed-down of the movements is visible. Picture (b) shows a array of dots, driven with full speed, with all described measures for synchronization implemented.

the basic operation of the stage. This approach is fast and easy extendable. A major drawback is the application specific syntax and the need to write filters for import and export. Since the scripting language is human readable, the packing density is quite bad (up to 50Bytes/command). Also the parsing of this files is not optimized. Both factors result in an import duration of several minutes for reasonably complex structures.

To extend the usability of the system an import filter for vector based formats was implemented. A commonly used format used in micro-processing is the GDSII-data format. Originally developed in the 70th by Calma, it is a streaming data format which arranges shapes in hierarchical order. Each structure is divided in cells (also called hierarchies) which is similar to 'groups' in modern graphic programs. Also each element is part of a layer. The decision for using the Calma format is based on common usage of the format in related industries like photomask services and the in-house e-beam lithography system, which also takes advantage of the GDSII data format. Structures produced procedural in Labview can also be imported and exported in binary format for later re-use.

4.3 Laser Ablation

If light is shone on a surface it interacts with the material. Fundamental interactions include absorption, transmission, reflection and scattering. A focused laser beam, like used in this setup can apply high fluences on the substrate. For example a beam with 1mJ pulse energy (pulse length 40ns) focused down on an area of 100x100μm^2 would have an intensity of 2.5$\frac{\mathrm{MW}}{cm^2}$ during the pulse.

In case of a homogeneous smooth surface the amount of transmitted and

reflected light underlies the Fresnel- Formulas

$$R_{\perp} = \frac{\sin^2(\phi_{inc} - \phi_{trans})}{\sin^2(\phi_{inc} + \phi_{trans})} \tag{4.6}$$

$$R_{\parallel} = \frac{\tan^2(\phi_{inc} - \phi_{trans})}{\tan^2(\phi_{inc} + \phi_{trans})} \tag{4.7}$$

$$T_{\perp} = \frac{\sin(2\phi_{inc})\sin(2\phi_{trans})}{\sin^2(\phi_{inc} + \phi_{trans})} \tag{4.8}$$

$$T_{\parallel} = \frac{\sin(2\phi_{inc} - 2\phi_{trans})}{\sin^2(\phi_{inc} + \phi_{trans})\cos^2(\phi_{inc} - \phi_{trans})} \tag{4.9}$$

where the angle of the incident beam ϕ_{inc} and the angle of the transmitted beam ϕ_{trans} are related by Snell's law (n_1 and n_2 are the complex indexes of refraction)

$$n_1 \sin(\phi_{inc}) = n_2 \sin(\phi_{trans}) \tag{4.10}$$

The transmitted light is successively absorbed inside the material according to Beer-Lambert's law. $I(x) = I_0 \exp(-\alpha x)$ where the absorption coefficient α is depending on the material and the wavelength. Thereby the absorption coefficient can vary in a wide range, for example at 1μm the absorption coefficient of fused silica is around $10^{-5} cm^{-1}$, while metals have a typical absorption of $10^6 cm^{-1}$. Since the absorption coefficient is proportional to the imaginary part of index of refraction, the amount of reflected light increases with increasing absorption coefficient.

Using sufficient energy it is possible to remove material by laser irradiation. The processes involved in ablation can be quite complex. Different models are suggested depending on the used wavelength, material and pulse duration. Especially the interaction between excimer laser and organic material shows different behavior compared to either the interaction with metals or the ablation by infrared lasers[33].

The basic model of ablation follows several phases. When the irradiation of the material starts, the laser energy is absorbed and transformed into local heating. Due to a gradient in the heating, a fraction of the heat is conducted

away, depending on the thermal conductivity of the material. With increased heating, the substrate locally starts to melt and finally vaporizes[14]. The fast time scales of the vaporization induces two effects. The ablated material is expanding in a plume, because of the pressure gradient of the vapor, also due to high temperatures reached in the vapor, thermal ionization generates a plasma[25]. Free electrons in the plasma absorb the laser radiation by inverse Bremsstrahlung, shielding the sample from further irradiation.

This model can describe the interaction of long pulses with metals. Since the typical time constant for thermalization of the electron gas with the lattice is around $10^{-13}s$, the heating can be seen as instantaneous in the case of ns pulses, like in the case of excimer lasers. Realistic models have to include other effects in addition, for example the decrease of reflectance of a metal close to the melting point or the changed surface morphology after a previous ablation pulse. With the availability of pulsed-amplified femtosecond lasers, it is possible to process metals by heating up the electrongas, before thermalization processes with the lattice occur [24].

This ablation models indicates, that ablation is dependend on various material constants (melting point, thermal conductivity, absorption, etc...). The model suggest aslo the existence of an ablation threshold. If the intensity is lower than this threshold, the material is able to dissipate the laser energy, before vaporisation of the material starts. In laser cleaning this effect is used, by choosing a fluence, that is higher than the ablation threshold for contaminants, but smaller than the threshold of the substrate.

For organic materials, models based on heating and vaporization break down in the case of excimer lasers. An ablation process that is based on local heating produces a zone around the ablation hole, where the material has been melted, but not ablated. Ablation done by excimer laser radiation in organic material does not show this effect, in contrast sharp edges are visible at the border of the ablated material[40].

To explain this behaviour, a model based on photothermal effects assumes that the UV radiation is directly absorbed into lattice vibrations, which thermally dissociates the polymer. While good consistency of this model can be demonstrated for soft UV radiation, investigation of ablation with laser wavelengths below 248nm suggest, that an additional photochemical component is involved, where the UV photons directly break bonds inside the polymer[29].

This different behaviour in the ablation process of excimer laser radiation, allows one to produce structures with sharp edges. While this is true for polymers and insulators[34], the fast thermalization of metals results in melting at the edges, reducing the quality of the cut.

One application of the system is to process organic nanofibers after the growth[7]. It was mentioned earlier, that organic nanofibers show gain narroring or random lasing. Quochi et al have shown, that the thermal breaks along a nanofiber reflect the wave and work as resonator. The excimer laser allows us to cut the nanofibers at a defined distance and create resonators not depending on thermal breaks. An important factor is the quality of the cut.

In the first series of experiments, the correlation of fluence and focus has been investigated on organic nanofibers directly on the muscovite mica substrate. In figure 4.15 a rectangular ablated area can be seen. While edge quality and removal of all material are the benchmark for a good cut, the underlying substrate should not be affected by the ablation.

Figure 4.16 shows the result of the quality of the cut with varying intensity. A high fluence results in a sharp cut with an edge quality of 400nm, but the underlying substrate starts to get affected. Lower intensities leave noticable amounts of material on the substrate, while also impairing the quality of the cut.

To estimate the influence of the optical alignment on the result, the sample was moved out of the focus. As can be seen in figure 4.17, the adjustment of the focus has a direct influence on the quality of the cut. It is remarkable that the region of the cut-away shows either residues of nanofibers, or the underlying subtrate is starting to get affected by the ablation process.

The latter results suggest, that to obtain a good cut-quality the influence of the mica substrate should be reduced. In a further series nanofibers have been transferred onto a UV-grade fused silica substrate. With a low absorbtion coefficient at 193nm, the difference in ablation threshold between the substrate and the organic nanofibers is bigger, allowing to selectivley remove the material.

Both focal distance and intensity of the laser pulse have been altered, to obtain the best possible cut. Figure 4.19 is an AFM image from a cut with

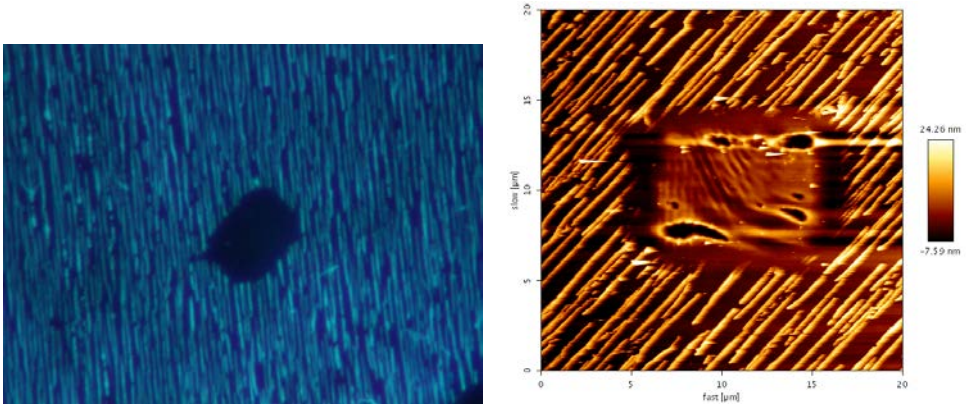

(a) (b)

Figure 4.15: Figure (a) shows a fluorescence image of a rectangular cut with a high intensity pulse. No fluorescent material remains on the surface. Figure (b) is an AFM image of the same region. It is clearly observable, that all fiber-material has been removed, but also that the substrate has been strongly affected. The shown measurements had been done by K. Thilsing-Hansen and M. Madsen [22].

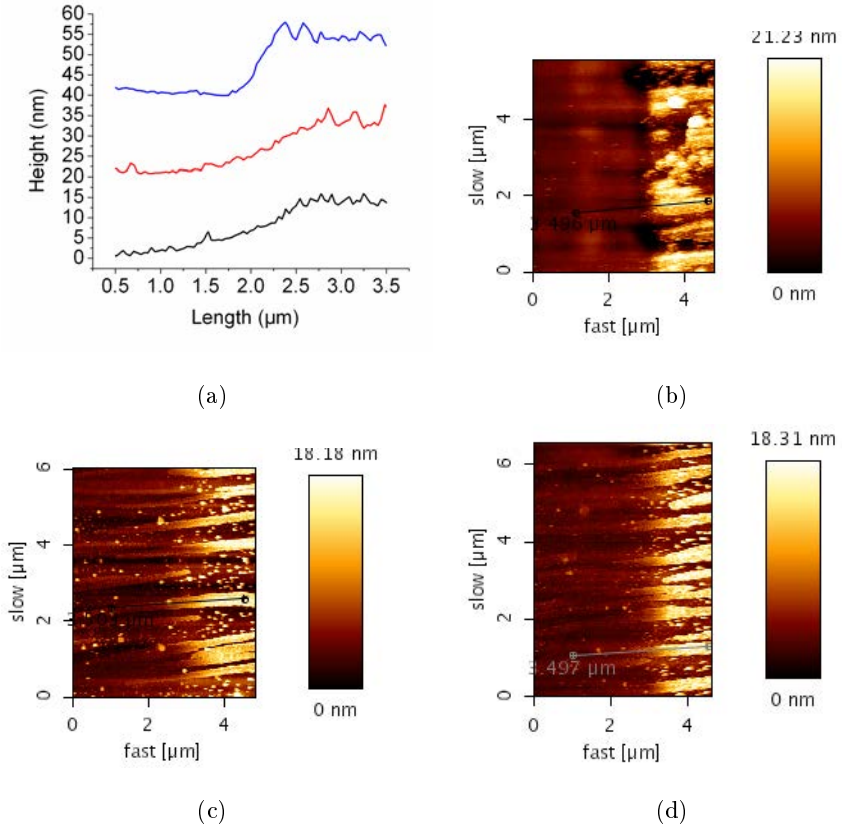

Figure 4.16: Ablation of organic nanofibers. Figure (b), (c) and (d) show the cut of organic nanofibers, with high, medium and low fluence. In figure (a) the cross-section of different cuts is compared. The shown measurements are based on work by K. Thilsing-Hansen and M. Madsen [22].

optimum parameters. All of the needle material has been removed in the region of the cut-away, as it can be seen from the AFM-phase image. The cut shows a slope below 400nm.

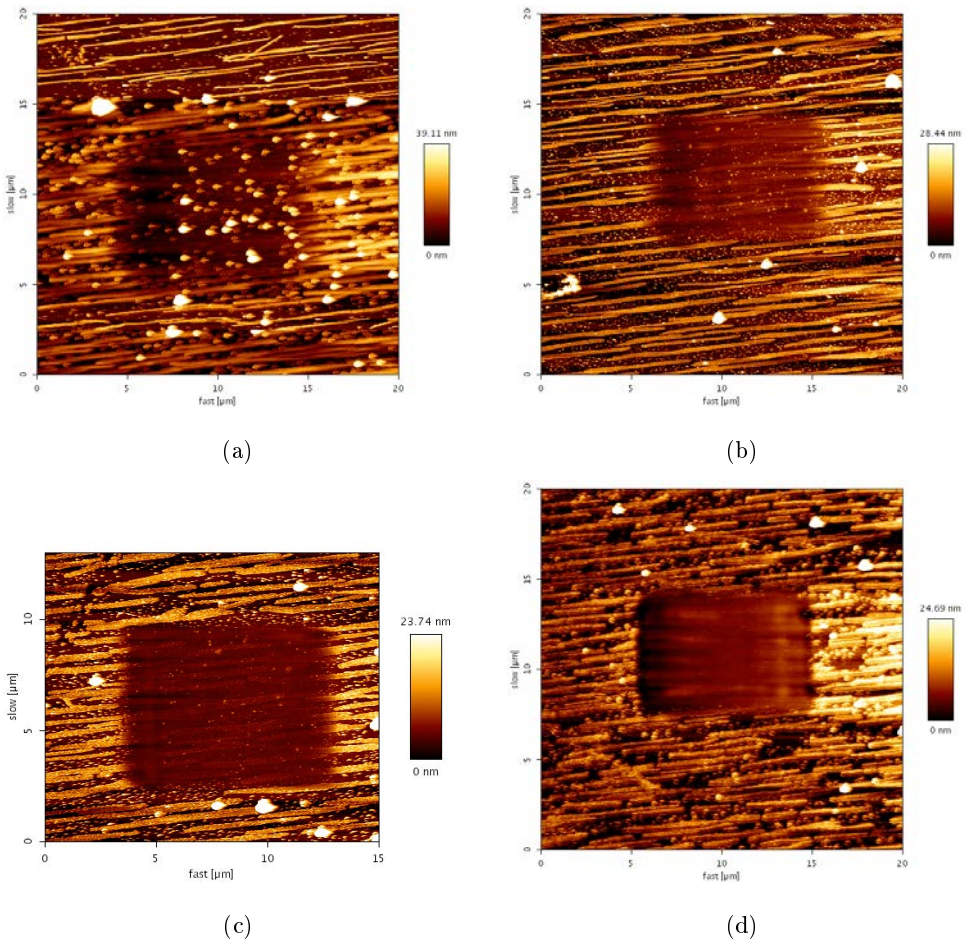

Figure 4.17: Effect of focus on the quality of the cut. Figure (a), (b), (c), (d), show -20μm, -10μm, 0μm, 10μm offset from the focal position. The shown measurements had been done by K. Thilsing-Hansen and M. Madsen [22].

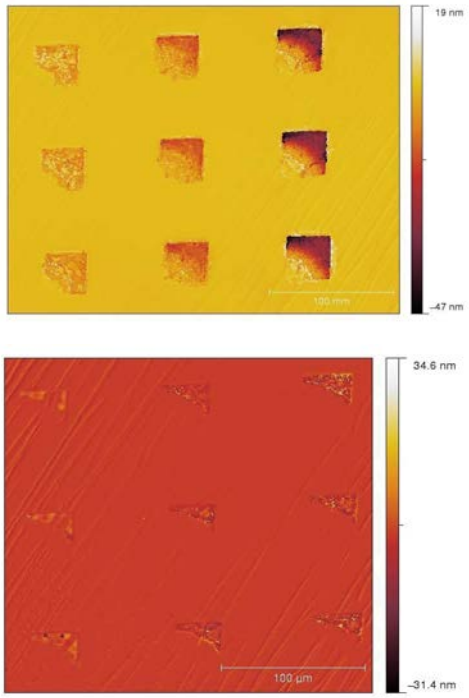

Figure 4.18: Interference microscopy images of laser-cutted organic nanofibers on fused silica.

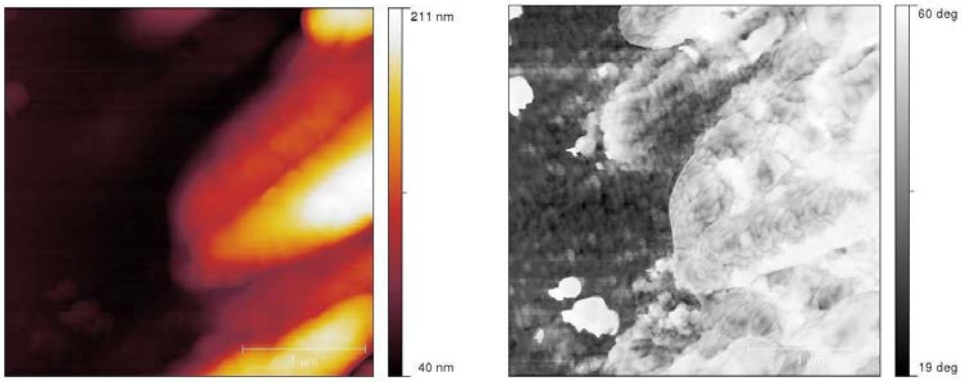

(a) (b)

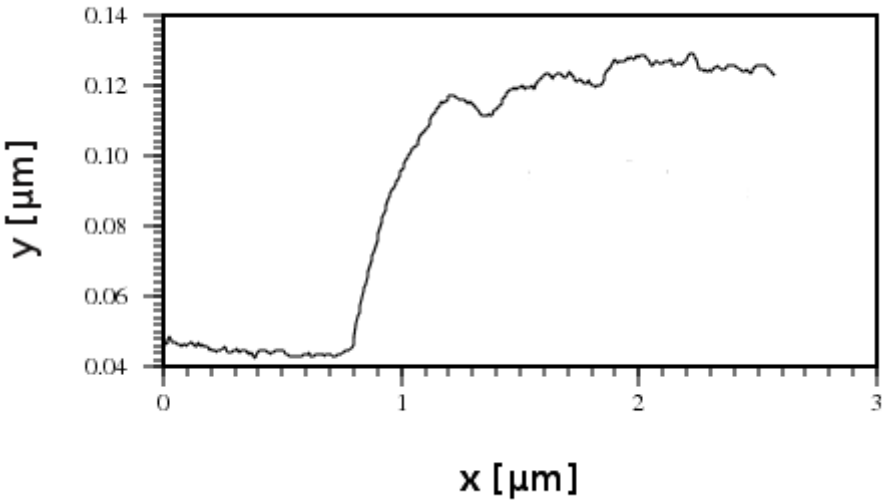

(c)

Figure 4.19: Laser-cut of organic nanofibers. Figure (a) - Close-up of cut fibers. The picture shows an AFM-height-image of the fiber end. The AFM was operated in tapping mode. Figure (b) AFM-phase image of the region. The phase information of the AFM signal depends on material properties. The image shows a clear shift in the signal from the area of fibers to the substrate, indicating a complete removal of all organic material. Figure (c) shows the cross-section of the cut of one needle.

4.4 Laser Engraving

To produce arbitrary structures, the laser beam was reduced by an aperture to produce a sharp cut in the material. By moving the stage, while ablating material, the system can be used as an optical stylus. The easy import of CAD drafted structures in the computer allows to have a versatile tool for rapid prototyping.

The resolution of structures produced with this method is limited by the accuracy of the stage and the spot size. To test the accuracy of the stage, and the production method, a pattern of parallel lines of 2μm was written over a distance of 5 mm. Since a typical application of this method is the production of masks that can be used with this system, all following structures are produced in a UV-grade fused silica substrate, covered with 50nm of chromium. The mask has been protected with a layer of 200nm magnesium fluoride.

The first substrates showed a problem with the quality of the ablation. The chromium film formed a smooth layer, without any visual defects. The illumination with small pencil sizes did not only remove chromium in the illuminated areas, but also the ablation of the chromium tended to be in flakes. The wiggling shape of the line pattern seen in figure 4.4 is caused by a combination of this effect and vibration of the sample and stage.

The problem of the ablation of flakes could be reduces by lowering the evaporation rate of the chromium layer. Also illumination with a bigger stencil reduces the effect of the flakes. The vibration could be reduced by improved fixing of the substrate and re-enforcement of the microscope optics.

This line test shows, that parallel lines can be accurateley produced over distances of several mm. The resolution of the stage is acceptable to produce lines with a spacing of less than 5 μm. Demagnified by the 15x objective, the

result is a final resolution of 330nm which is comparable to the diffraction limit of the objective with 193nm.

Applying the laser radiation from the front side of the object has some consequences on the quality of the produced mask. On the one hand the geometrical configuration is aligned in a way, that the laser is illuminating the sample from above. The evaporated material is ejected from the sample in the direction of the beam. Gravitation and laser induced plasma ricochets back at the surface as debris. Another inconvenience is that mis-set intensities can damage the underlying optical surface. Since the substrate is transparent for the UV-radiation, it is possible to focus the beam passing through the substrate, ablating the thin layer from the back-side.

In figure 4.21 two structures are shown, where one is ablated from the front-side, the other one is ablated from the back. The pictures are taken by dark-field microscopy, enhancing defects on the surface. While the ablated areas are not uniformly ablated, the ablated lines in figure 4.21(b) show residual material or damages.

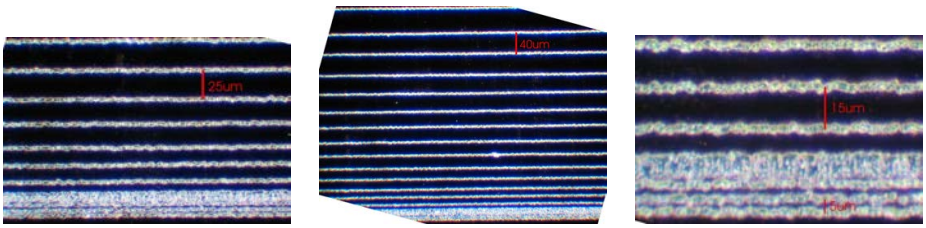

Figure 4.20: Engraving of 2μm thick lines with increasing separation between lines. Chromium, which has been evaporated on a fused silica substrate, has been removed, by a spot of 2μm. The overlap of the high-resolution lines in figure (c) is due to an accidential double illumination in that region.

4.5 Single-Shot structure Formation

In the last section, it was demonstrated how to utilize the excimer laser to selectively remove chromium from a covered substrate. By controlling the movement of the laser, it is possible to rapidly produce masks, with a resolution below 5μm. These masks can then again be used to produce structures, by imaging them on the sample with a de-magnification of 15x or 25x, depending on the objective.

This technique allows one to produce structures with maximum resolution. To test the performance, manufactured mask with various grid sizes has been used. This offers various line and grid patterns with different grid constants. Figure 4.23 shows SEM pictures of a line grid demagnified on a gold-covered silicon wafer. The lattice choosen for demagnification has a grid constant of 13.3 $\frac{1}{\text{mm}}$, which is equal to a spacing of 75μm between lines.

The resulting structures show straight edges of the bars, which are tattered in a region of around 300 nm. As described in section 4.3, the heat

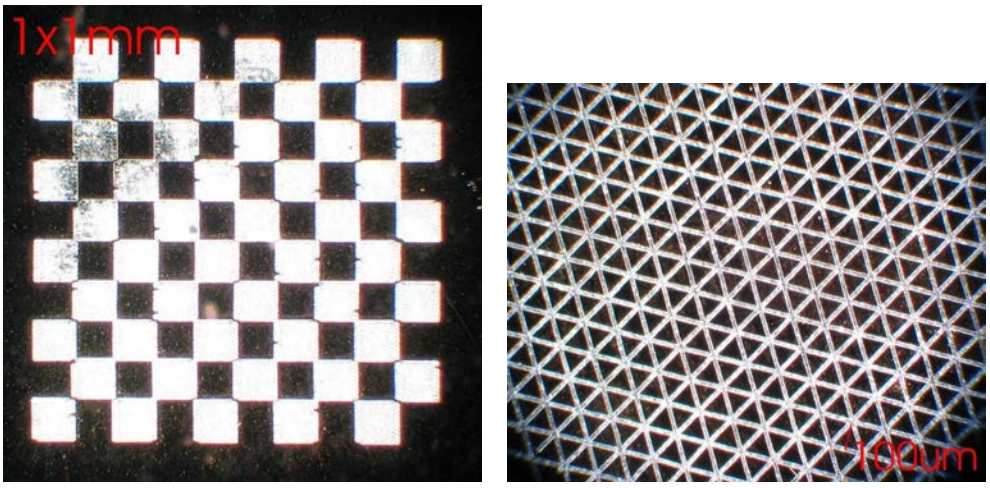

Figure 4.21: Comparison between front-side ablated ((a)) and back-side ablated ((b)) structures.

dissipation in metals is high, and the energy is absorbed collectively in the electronical system. The resulting ablation mechanism is governed by local heating and the transition from the solid phase through the liquid phase to vapour phase. It can be clearly seen, that the quality of the structures in this system is determinined by the melting of the metal around the edges.

To investigate the resolution limit of this technique, a grid with a lattice constant of $66\frac{1}{mm}$ was imaged onto a BK7 glas sample. The image of this lattice would have a linewidth of 1μm on the sample. The structure size was further reduced by using the obscuration of the microscope objective. As mentioned in section 4.2.3, the blocked area in the middle has a different MTF than illumination in one of the segments. This can be illustrated also with other means. The mask splits the laser beam in the direct propagating beam and the higher diffraction orders. The entrance aperture of the objective only allows the direct beam and the first-order diffracted beam to enter the microscope objective. Inside the objective the direct beam is blocked by the obscured part.

The angles of the first diffraction order beams to the optical axis is given

Figure 4.22: Image of a produced mask for excimer ablation. The fused silica sustrate is 25mm x 25mm in dimension, and divided in 9 different segments of each 5mm x 5mm.

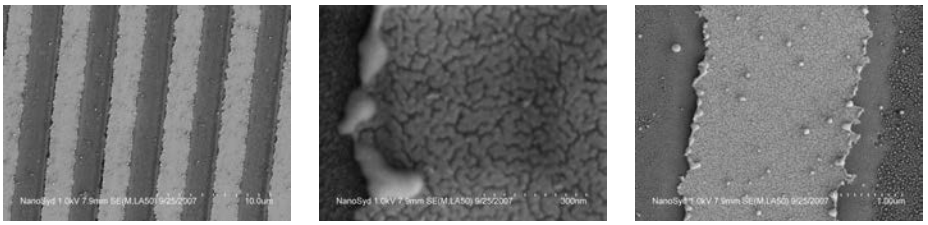

Figure 4.23: Structure formation in a 50nm thick gold film, evaporated on a silicon wafer

by

$$\sin\Theta_{\pm} = \frac{\lambda}{d} \tag{4.11}$$

where d is the distance between the slits in the mask. After passing the objective, the two beams are leaving the objective in a new angle $\Theta'_{\pm}$ depending on the magnification M:

$$\sin\Theta'_{\pm} = M\sin\Theta_{\pm} = \frac{M\lambda}{d} \tag{4.12}$$

In the focus, the two beams interfere. The intensity distribution of the two waves is described as (where z is the the direction of the optical axis):

$$E_{focus} = E_{\pm}\left(e^{i\frac{2\pi}{\lambda}\left(\cos\Theta'_{\pm}z+\sin\Theta'_{\pm}x\right)} + e^{i\frac{2\pi}{\lambda}\left(\cos\Theta'_{\pm}z-\sin\Theta'_{\pm}x\right)}\right) \tag{4.13}$$

$$= 2E_{\pm}e^{i\cos(\frac{2\pi}{\lambda}\Theta'_{\pm})z}\sin(\frac{2\pi}{\lambda}\sin\Theta'_{\pm}x) \tag{4.14}$$

$$I(x) = 2I_{\pm}\sin^2(\frac{2\pi M}{d}x) \tag{4.15}$$

Since $\sin^2$ has a maximum every π, we get an intensity distribution which has a distance between two maxima of $\frac{d}{2M}$, which would result in the used configuration in a distance of 500nm.

Structures produced in that way can be seen in figure 4.24. The produced ripples have a width of around 250nm, which is around the diffraction limit for the used objective.

The masks produced with the techniques described in section 4.4, enable one to rapidly prototype layouts with high resolution. As an example, a

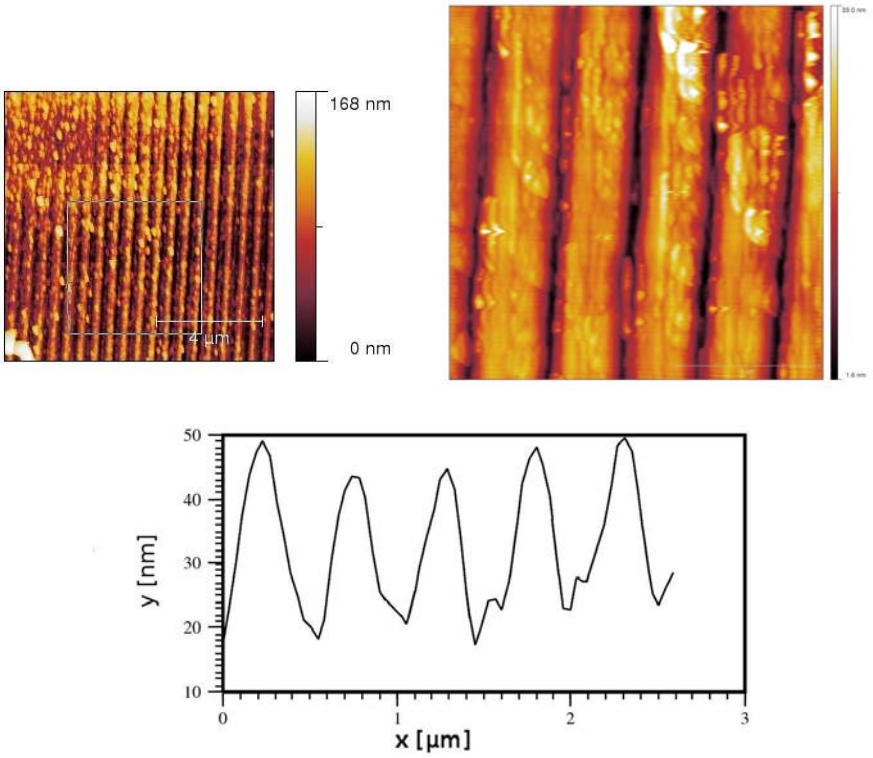

Figure 4.24: Structure formation in BK7 glas. A 15μm grid has been demagnified on the surface. A separation of 500nm is reached, by blocking out the zeroth order beam. The resulting features have a mean width below 250nm.

Fresnel zone plate has been produced with the excimer station. The layout of the lens was produced line by line, as can be seen in figure 4.25. The line by line drawing of the mask generates a coarse approximation of the lens, which can be fast produced. It is possible to produce a higher quality layout of the Fresnel mask by ablating the zones circle by circle. This technique was choosen to investigate the import of picture files in the setup and rastering them. Both in the layout and also in the mask, Moire patterns are visible.

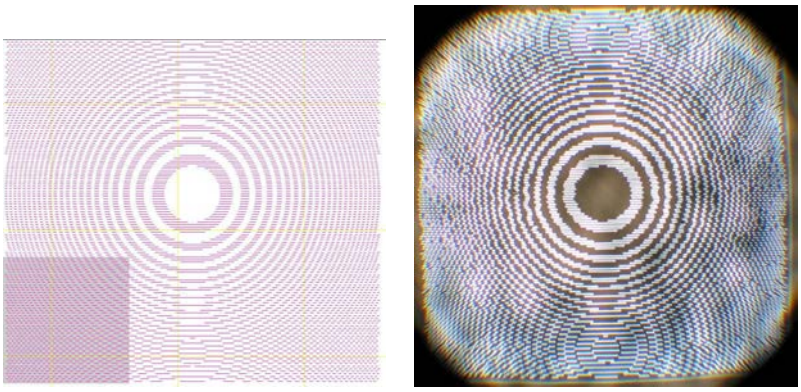

(a) (b)

Figure 4.25: Production of a simple Fresnel mask Figure (a) shows the layout for the lens. The dark colored square is 1mm x 1mm in size. The Moire pattern originates from rastering the images in lines. Figure (b) shows the produced mask from the template. The mask is shot on an UV-grade fused silica substrate covered with 60nm of Chromium and 500nm Of MgF_2 as protective layer.

The mask was imaged down on chromium covered glass substrates. Compared to gold, chromium has a higher melting point and a lower vaporization temperature, while having similar heat capacities and heat of vaporization. The melting on the border is reduced, but chromium shows the tendency of ablating in flocks of material, reducing the quality of the structure. Since the flocks can vary in size, the fluence necessary to ablate a single flock, is reduced by the mismatch between the illuminated area and the actual size of the ablated flock. This behaviour can be observed in figure 4.26. By

illuminating the substrate with high fluences, large features are reproduced precisely, but smaller feature sizes are undefined due to the grains of the ablation. Reducing the intensity, the smaller features are better imaged, but on some areas the intensity is not sufficent to ablate enough material.

Better results can be obtained by structuring polymers. In figure **??**, the same mask has been imaged on an acryl-glass substrate. The quality of the structure formation is higher compared to the case of the chromium coverd substrate. This imaging technique allows one to reproduce a series of these structures. The throughput in production is only limited by the repetition rate of the laser and the maximum velocity of the translational stages.

Figure 4.27 shows a section of an large array of Fresnel lenses, that had been produced in that way. The Fresnel lenses are separated by 150 μm and the process time needed for each lens has been 0.3s. Using this method it offers great advantages for fast prototyping, but due to the serial way of production structures, the throughput can be low compared to other techniques. The production of a 15mm by 15mm large area took around one hour to finish.

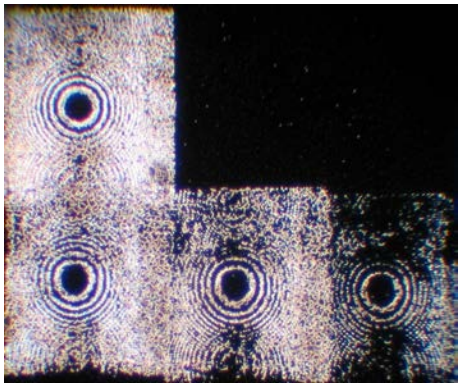

Figure 4.26: Single shot formation of structures in a chromium covered BK7 substrate. Between the different shots, the intensity of the laser has been changed.

Another method to produce structures with excimer laser is by bringing a substrate in direct proximity of the mask, without using an objective. This does not allow to produce with the same high resolution that can be achieved by utilizing a high NA objective, but the processable area is large. In figure 4.28 a line pattern is produced in acryl glass this way. This method has been tested to show its feasability, but did not give promising results. Due to the unfocused laser beam used in this method, only easy-to-ablate materials can be processed. The intensity of the laser has to be higher, resulting in faster degeneration of the mask quality. Also the ablated material is successively contaminating the mask.

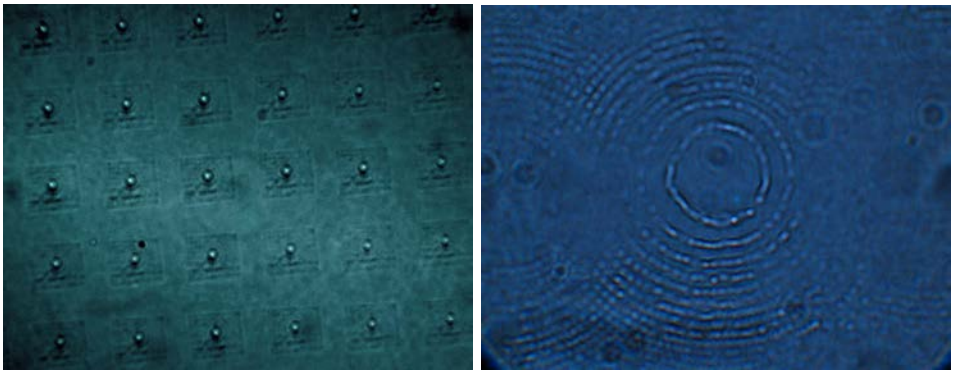

(a) (b)

Figure 4.27: Array of single-shot produced Fresnel lenses in acryl glas. The array is illuminated from behind and the image is taken in the focal plane of the Fresnel lenses.

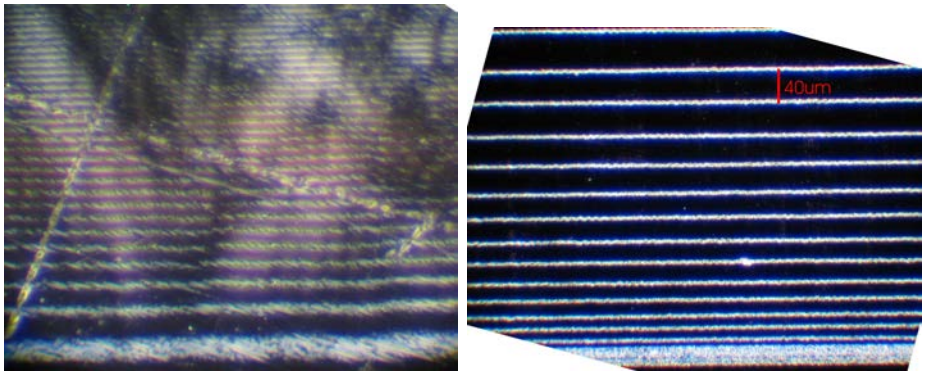

Figure 4.28: Production of line structures by proximity illumination. The mask (right) was brought in contact with a acryl glass substrate(left). Direct illumination with 193nm laser light ablated the uncovered parts of the acryl glass.

Chapter 5

Conclusion

In this thesis we have presented how organic nanofibers can have a role in future application in integrated optics. It has been demonstrated that they can act as light guiding elements. Due to their dimensions, they have unique properties. Recent research on evanescent field sensors, as for example in [21], are limited by the volume probed with the evanescent wave. A model to numerical calculate the field distribution has been demonstrated. It showed, that the evanescent field strongly depends on the used geometry of the nanofibers.

The optimization of the evanescent field is limited by the interaction of the fiber and the substrate. It has been shown that by reducing the dimensions of the cross-section, the amount of energy in the evanescent field can be enlarged, but as counteracting process, the evanescent field is mostly confined in the region of the supporting substrate. The simulation suggests an optimum for the amount of the evanescent field energy which coincides with the typical growth-dimensions of the substrate.

The same techniques have been applied to describe the system of two aggregates. It has been demonstrated that two fibers are coupling if they are in each others proximity. In the case of some 10 nm, they are coupled so strongly, that only a common propagating mode exist. In intermediate separation distances up to around 2 microns, the fibers guide in separate modes, but these are influencing each other in a way, that part of the excitation in one fiber is transferred to the near-by fiber. These cross-talking problems are a fundamental limitation in terms of packing densities in future applications.

Another part of the theoretical investigating was centred about the influence of altering the morphology of a nanofiber along its axis. It was shown, that by tapering the fiber, a local enhancement of the evanescent field can be produced.

In the following parts of this thesis, we have demonstrated how to change

the morphology of organic nanofibers to realize the theoretically predicted effects. One approach takes direct influence on the growth of the organic nanofibers. It was demonstrated, that organic nanofibers can also be grown from functionalized molecules. The nanofibers made from this new material show a variety of cross-sectional shapes, like square or triangular cross-sections.

Another approach was to treat the substrate before growth. By evaporation of gold on the mica surface, it is possible to influence the growth of the fibers. The evaporated gold offers for low coverages an additional control mechanism to define the length of the nanofibers. In the case of high coverage it is possible to obtain an interlinked, net-like structure of organic nanofibers.

For realizing structuring of organic nanofibers along their propagation axes, we have introduced the method of excimer laser material treatment. In the scope of this thesis, such a system has been implemented. This implementation covered the set-up of the different components. Additionally a software solution for integrated control of the system has been developed. The software enables the user to manually control each aspect of the system. By implementation of the GDSII data format and other interfaces, it is possible to feed the system with layouts and to produce complex structures.

It has been demonstrated that this system can be used to cut organic nanofibers. This process can be adjusted to selectively remove the material of the nanofiber, without altering the underlying substrate. The quality of the cut has been investigated and it was shown, that it is possible to define the end-facet of a single nanofiber with a resolution of around 400nm

In the following it has been shown, that the system can produce structures down to the diffraction limited feature size of 250nm by single shot ablation.

The usability of the system for rapid prototyping has been demonstrated on the example of a Fresnel zone plate. It has been demonstrated that the same system can be used to produce masks and also to use exactly these masks to generate high resolution structures on substrates.

Acknowledgment

The work done in this thesis would not had been possible without the aid of many people. At first I would like to thank the European research and trainings network Fastnet, which founded two years this PhD position. Additional financing of this position was given by the University of Southern Denmark.

I thank Prof. John Weiner, who supervised my stay at the University of Toulouse. Many fruitful discussions have enriched my understanding of near-field optics. During my time in Toulouse Gaëtan Lévêque introduced me to the differential theory of gratings and made it possible to compare this technique with my finite element simulation. I want to thank Prof. Morten Willatzen for his support on technical issues of implementing the finite element methods. Thanks to the help of Dr.Sci. Vladimir Bordo it was possible to elaborate analytical models of near-field light propagation.

I want to thank Manuela Schieck and Prof. Al-Shamery from the University of Oldenburg for functionalizing the organic molecules. Assoc. Prof. Frank Balzer offered me help with deep knowledge on the growth mechanisms of organic nanofibers. I want to thank Morten Madsen and Kasper Thilsing-Hansen for their help with the cutting of nanofibers.

I want to thank Torben Sørensen, Danny Kyrping and Darios N. Rizi for technical assistance in manufacturing and installing components for the system.

I would like to express my deepest appreciation for Prof. H.-G. Rubahn, the supervisor of this thesis. He helped me on so many issues during my PhD time, that it would go beyond the scope of this acknowledgment.

Further tanks to all my colleagues at NanoSYD, IFK and MCI.

Publications

- "Nanofibers from functionalized para-phenylene molecules", M.Schiek, A. Luetzen, R. Koch, K. Al Shamery, F. Balzer, R. Frese and H.-G. Rubahn, Appl.Phys. Lett.86(2005)153107."Nanofibers from functionalized para-phenylene molecules", M.Schiek, A. Luetzen, R. Koch, K. Al Shamery, F. Balzer, R. Frese and H.-G. Rubahn, Appl.Phys. Lett.86(2005)153107.

- Tayloring the growth of p-6P nanofibres by ultrathin Au layers: an organic-metaldielectric model system", F.Balzer, L.Kankate, H. Niehus, R.Frese, C.Maibohm and H.-G. Rubahn, Nanotechnology 17(2006)984.

- "Bottom-up tailoring of photonic nanofibers", F.Balzer, M.Madsen, R.Frese, M. Schiek, T. Tamulevicius, S.Tamulevicius and H.-G. Rubahn, SPIE 6883(2008).

- "Spatial emission characteristics of waveguiding organic nanofibers", R. Frese, C.Maibohm, J.Gravesen, M.Willatzen and H.-G.Rubahn, DPG Fruehjahrstagung, Berlin 2005; CAMS, Heidelberg April 2005.

- "Functionalized para-phenylene nanofibers", F.Balzer, K.Al-Shamery, A.Luetzen, M.- Schiek, R. Frese and H.-G.Rubahn, DPG Fr¨uhjahrstagung, Berlin 2005.

- "Organic nanofibers from functionalized para-phenylene molecules", M.Schiek, A. Luetzen, K. Al-Shamery, F. Balzer, R. Frese and H.-G. Rubahn, Workshop on 2- and 3-D organic nanostructures, Linz (2005).

- "Waveguiding in organic nanofibers: measurements and simulations", Ralf Frese, J. Brewer, C. Maibohm, HJ. Gravesem, M. Willatzen and H.-G. Rubahn, Workshop on 2- and 3-D organic nanostructures, Linz (2005).

- "Nanofibers from functionalized para-phenylene molecules", M.Schiek, A. Luetzen, K.Al-Shamery, F. Balzer, R. Frese and H.-G. Rubahn, ECOSS 2005 (2005).

- "UV-laser treatment in the nanodomain: forming of organic nanofibers", F. Balzer, R.Frese, K. Thilsing-Hansen, J. Ihlemann and H.-G. Rubahn, LAMP06, Kyoto (2006).

- "Nanosensors based on organic nanofibers", M.Madsen, N.L.Andersen and H.-G. Rubahn, Advanced 102 "Cutting and patterning of organic nanofibers",

F. Balzer, R. Frese, M.Madsen, K. Thilsing-Hansen and H.-G. Rubahn, Nanofair, Karlsruhe, 21-22.11. (2006).

- "Ultrafast organic nanofiber dynamics", K. Thilsing-Hansen, R. Frese and H.-G.Rubahn, DOPS meeting Risoe, 2007.

List of Figures

Bibliography

[1] Arti Agrawal and Anurag Sharma. Perfectly matched layer in numerical wave propagation: Factors that affect its performance. *Appl. Opt.*, 43(21):4225–4231, 2004.

[2] A. Andreev, F. Quochi, F. Cordella, A. Mura, G. Bongiovanni, H. Sitter, G. Hlawacek, C. Teichert, and N. S. Sariciftci. Coherent random lasing in the deep blue from self-assembled organic nanofibers. *Journal of Applied Physics*, 99(3):034305–+, February 2006.

[3] F. Balzer. Nonlinear optics of hexaphenyl nanofibers. *Chemical Physics Letters*, 368:307–312, January 2003.

[4] F. Balzer, V. G. Bordo, R. Neuendorf, K. Al Shamery, A. C. Simonsen, and H.-G. Rubahn. Organic nanofibers: a new window to optics of ultrasmall aggregates. In R. Vajtai, X. Aymerich, L. B. Kish, and A. Rubio, editors, *Nanotechnology. Edited by Vajtai, Robert; Aymerich, Xavier; Kish, Laszlo B.; Rubio, Angel. Proceedings of the SPIE, Volume 5118, pp. 263-270 (2003).*, volume 5118 of *Presented at the Society of Photo-Optical Instrumentation Engineers (SPIE) Conference*, pages 263–270, April 2003.

[5] F. Balzer, V. G. Bordo, A. C. Simonsen, and H.-G. Rubahn. Isolated hexaphenyl nanofibers as optical waveguides. *Applied Physics Letters*, 82:10–+, January 2003.

[6] F. Balzer, V. G. Bordo, A. C. Simonsen, and H.-G. Rubahn. Optical waveguiding in individual nanometer-scale organic fibers. *Physical Review B*, 67(11):115408–+, March 2003.

[7] F. Balzer, J. Ihlemann, A. C. Simonsen, and H.-G. Rubahn. UV laser cutting of organic nanofibers. In E. G. Johnson, G. P. Nordin, and T. J. Suleski, editors, *Micromachining Technology for Micro-Optics and Nano-Optics III. Edited by Johnson, Eric G.; Nordin, Gregory P.; Suleski, Thomas J. Proceedings of the SPIE, Volume 5720, pp. 165-172 (2005).*, volume 5720 of *Presented at the Society of Photo-Optical Instrumentation Engineers (SPIE) Conference*, pages 165–172, January 2005.

[8] F. Balzer, L. Kankate, H. Niehus, R. Frese, C. Maibohm, and H.-G. Rubahn. Tailoring the growth of p-6P nanofibres using ultrathin Au layers: an organic metal dielectric model system. *Nanotechnology*, 17:984–991, February 2006.

[9] F. Balzer, L. Kankate, H. Niehus, and H.-G. Rubahn. Tailoring of organic nanofiber growth for a new type of waveguides. In J. G. Grote, F. Kajzar, and N. Kim, editors, *Organic Photonic Materials and Devices VIII. Edited by Grote, James G.; Kajzar, Francois; Kim, Nakjoong. Proceedings of the SPIE, Volume 6117, pp. 20-27 (2006).*, volume 6117 of *Presented at the Society of Photo-Optical Instrumentation Engineers (SPIE) Conference*, pages 20–27, March 2006.

[10] F. Balzer, M. Madsen, R. Frese, M. Schiek, T. Tamulevicius, S. Tamulevicius, and H.-G. Rubahn. Bottom-up tailoring of photonic nanofibers. In *Advanced Fabrication Technologies for Micro/Nano Optics and Photonics. Edited by Suleski, Thomas J.; Schoenfeld, Winston V.; Wang, Jian Jim. Proceedings of the SPIE, Volume 6883, pp. 68830T-68830T-8 (2008).*, volume 6883 of *Presented at the Society of Photo-Optical Instrumentation Engineers (SPIE) Conference*, February 2008.

[11] F. Balzer and H.-G. Rubahn. Laser-controlled growth of needle-shaped organic nanoaggregates. *Nano Letters*, 2(7):747–750, 2002.

[12] A. Bendali and P. Guillaume. Non-reflecting boundary conditions for waveguides. *Mathematics of Computation*, 68:123–144, 1999.

[13] J.-P. Berenger. A Perfectly Matched Layer for the Absorption of Electromagnetic Waves. *Journal of Computational Physics*, 114:185–200, October 1994.

[14] A. Bogaerts. Laser ablation for analytical sampling: what can we learn from modeling? *Spectrochimica Acta*, 58:1867–1893, November 2003.

[15] V. G. Bordo. Light scattering from a nanofiber: Exact numerical solution of a model system. *Physical Review B*, 73(20):205117–+, May 2006.

[16] C.H. Borgins, F.E. amd Papas. *Electromagnetic Waveguides and Resonators in in. Handbuch der Physik, vol. 16, Berlin.*

[17] L. C. Botten and M. Cadilhac. *Electromagnetic theory of gratings.* Topics in Current Physics, Berlin: Springer, 1980, edited by Petit, R., 1980.

[18] A. C. Boucouvalas and C. D. Papageorgiou. Cutoff frequencies in optical fibers of arbitrary refractive index profile using the resonance technique. *IEEE Journal of Quantum Electronics*, 18:2027–2031, December 1982.

[19] J. Brewer, H. H. Henrichsen, F. Balzer, L. Bagatolli, A. C. Simonsen, and H.-G. Rubahn. Nanofibers made to order: free floating, transferred and gel-packed organic nanoaggregates. In E. A. Dobisz and L. A. Eldada, editors, *Nanoengineering: Fabrication, Properties, Optics, and Devices II. Edited by Dobisz, Elizabeth A.; Eldada, Louay A. Proceedings of the SPIE, Volume 5931, pp. 250-257 (2005).*, volume 5931 of *Presented at the Society of Photo-Optical Instrumentation Engineers (SPIE) Conference*, pages 250–257, August 2005.

[20] J. Brewer, C. Maibohm, L. Jozefowski, L. Bagatolli, and H.-G. Rubahn. A 3D view on free-floating, space-fixed and surface-bound para-phenylene nanofibres. *Nanotechnology*, 16:2396–2401, October 2005.

[21] Francesco Dell'Olio and Vittorio M. Passaro. Optical sensing by optimized silicon slot waveguides. *Opt. Express*, 15(8):4977–4993, 2007.

[22] M. Madsen K. Thilsing-Hansen H.-G. Rubahn F. Balzer, R. Frese. Uv-laser treatment in the nanodomain: Forming of organic nanofibers. *Journal of Laser Micro/Nanoengeneering*, 2006.

[23] W. Freude, H.-H. Yao, and Z.-J. He. Propagation constant and waveguide dispersion of single-mode fibers measured from the far-field. *Journal of Lightwave Technology*, 6:318–+, 1988.

[24] G. Hlawacek, Q. Shen, C. Teichert, R. Resel, and D. M. Smilgies. Controlling molecular orientation of OMBE grown 6P thin films on mica(0 0 1). *Surface Science*, 601:2584–2587, July 2007.

[25] J. Ihlemann, F. Beinhorn, H. Schmidt, K. Luther, and J. Troe. Plasma and plume effects on UV laser ablation of polymers. In C. R. Phipps, editor, *High-Power Laser Ablation V. Edited by Phipps, Claude R. Proceedings of the SPIE, Volume 5448, pp. 572-580 (2004).*, volume 5448 of *Presented at the Society of Photo-Optical Instrumentation Engineers (SPIE) Conference*, pages 572–580, September 2004.

[26] John David Jackson. *Classical Electrodynamics*. Wiley, 1998.

[27] L. Kankate, F. Balzer, H. Niehus, and H.-G. Rubahn. From clusters to fibers: Parameters for discontinuous para-hexaphenylene thin film growth. *Journal of Chemical Physics*, 128(8):084709–+, February 2008.

[28] J. Kjelstrup-Hansen, P. Bøggild, and H.-G. Rubahn. Charge Injection and Transport in Organic Nanofibers. *Journal of Physics Conference Series*, 61:565–569, March 2007.

[29] S. Küper, J. Brannon, and K. Brannon. Threshold behavior in polyimide photoablation: Single-shot rate measurements and surface-temperature modeling. *Applied Physics A: Materials Science & Processing*, 56:43–50, January 1993.

[30] M. Lohmeyer. Wave-matching method for mode analysis of dielectric waveguides, 1997.

[31] D. Marcuse. *Theory of dielectric optical waveguides.* New York, Academic Press, Inc., 1974. 267 p., 1974.

[32] F. Quochi, F. Cordella, A. Mura, G. Bongiovanni, F. Balzer, and H.-G. Rubahn. Gain amplification and lasing properties of individual organic nanofibers. *Applied Physics Letters*, 88(4):041106–+, January 2006.

[33] H.-G. Rubahn. *Laser Applications in Surface Science and Technology.* Laser Applications in Surface Science and Technology, by Horst-Günter Rubahn, pp. 346. ISBN 0-471-98450-7. Wiley-VCH , April 1999., April 1999.

[34] K. Rubahn, J. Ihlemann, and H.-G. Rubahn. Excimer laser sputtering of mica surfaces: Mechanisms and applications. *Journal of Applied Physics*, 86:2847–2855, September 1999.

[35] M. Schiek, A. Lützen, K. Al-Shamery, F. Balzer, and H.-G. Rubahn. Nanofibers from methoxy functionalized para-phenylene molecules. *Surface Science*, 600:4030–4033, September 2006.

[36] D. Schneider, T. Rabe, T. Riedl, T. Dobbertin, M. Kröger, E. Becker, H.-H. Johannes, W. Kowalsky, T. Weimann, J. Wang, and P. Hinze. Organic solid-state lasers based on sexiphenyl as active chromophore. *Journal of Applied Physics*, 98(4):043104–+, August 2005.

[37] E. K. Sharma, I. C. Goyal, and A. K. Ghatak. Calculation of cutoff frequencies in optical fibers for arbitrary profiles using the matrix method. *IEEE Journal of Quantum Electronics*, 17:2317–2321, December 1981.

[38] J. M. Simon and R. A. Depine. Differential theory of gratings: answer to an objection on its validity for TM polarization: comment. *Journal of the Optical Society of America A*, 5:1790–+, October 1988.

[39] E. Snitzer. Cylindrical Dielectric Waveguide Modes. *Journal of the Optical Society of America (1917-1983)*, 51:491–+, May 1961.

[40] R. Srinivasan. Ablation of polymers and biological tissue by ultraviolet lasers. *Science*, 234:559–565, October 1986.

[41] Fred Vermolen. Introduction into finite elements, 2005.

[42] Greg von Nessi. elementary theoratical methods in pde. electronical available, 2005.

[43] W. Walter. *Gewöhnliche Differntialgleichungen*. Springer, 1992.

[44] A. J. Ward. Refraction and geometry in Maxwell's equations. *Journal of Modern Optics*, 43:773–793, April 1996.